



Luminous Millimeter, Radio, and X-Ray Emission from ZTF 20acigmel (AT 2020xnd)

Anna Y. Q. Ho^{1,2}, Ben Margalit^{3,13}, Michael Bremer⁴, Daniel A. Perley⁵, Yuhan Yao⁶, Dougal Dobie^{7,8},
David L. Kaplan⁹, Andrew O'Brien⁹, Glen Petitpas¹⁰, and Andrew Zic^{11,12}

¹ Department of Astronomy, University of California, Berkeley, 501 Campbell Hall, Berkeley, CA, 94720, USA; annayqho@berkeley.edu

² Miller Institute for Basic Research in Science, 468 Donner Lab, Berkeley, CA 94720, USA

³ Astronomy Department and Theoretical Astrophysics Center, University of California, Berkeley, Berkeley, CA 94720, USA

⁴ Institut de Radio Astronomie Millimétrique (IRAM), 300 rue de la Piscine, F-38406 Saint Martin d'Hères, France

⁵ Astrophysics Research Institute, Liverpool John Moores University, IC2, Liverpool Science Park, 146 Brownlow Hill, Liverpool L3 5RF, UK

⁶ Cahill Center for Astrophysics, California Institute of Technology, MC 249-17, 1200 E California Boulevard, Pasadena, CA, 91125, USA

⁷ Centre for Astrophysics and Supercomputing, Swinburne University of Technology, Hawthorn, Victoria, Australia

⁸ ARC Centre of Excellence for Gravitational Wave Discovery (OzGrav), Hawthorn, VIC 3122, Australia

⁹ Department of Physics, University of Wisconsin-Milwaukee, P.O. Box 413, Milwaukee, WI 53201, USA

¹⁰ Harvard-Smithsonian Center for Astrophysics, 60 Garden Street, Cambridge, MA 02138, USA

¹¹ ATNF, CSIRO Space and Astronomy, PO Box 76, Epping, New South Wales 1710, Australia

¹² Department of Physics and Astronomy, and Research Centre in Astronomy, Astrophysics and Astrophotonics, Macquarie University, NSW 2109, Australia

Received 2021 October 11; revised 2022 January 21; accepted 2022 January 23; published 2022 June 22

Abstract

Observations of the extragalactic ($z = 0.0141$) transient AT 2018cow established a new class of energetic explosions shocking a dense medium, producing luminous emission at millimeter and submillimeter wavelengths. Here we present detailed millimeter- through centimeter-wave observations of a similar transient, ZTF 20acigmel (AT 2020xnd), at $z = 0.2433$. Using observations from the Northern Extended Millimeter Array and the Very Large Array, we model the unusual millimeter and radio emission from AT 2020xnd under several different assumptions and ultimately favor synchrotron radiation from a thermal electron population (relativistic Maxwellian). The thermal electron model implies a fast but subrelativistic ($v \approx 0.3c$) shock and a high ambient density ($n_e \approx 4 \times 10^3 \text{ cm}^{-3}$) at $\Delta t \approx 40$ days. The X-ray luminosity of $L_X \approx 10^{43} \text{ erg s}^{-1}$ exceeds simple predictions from the radio and UVOIR luminosity and likely has a separate physical origin, such as a central engine. Using the fact that month-long luminous ($L_\nu \approx 2 \times 10^{30} \text{ erg s}^{-1} \text{ Hz}^{-1}$ at 100 GHz) millimeter emission appears to be a generic feature of transients with fast ($t_{1/2} \approx 3$ days) and luminous ($M_{\text{peak}} \approx -21$ mag) optical light curves, we estimate the rate at which transients like AT 2018cow and AT 2020xnd will be detected by future wide-field millimeter transient surveys such as CMB-S4 and conclude that energetic explosions in dense environments may represent a significant population of extragalactic transients in the 100 GHz sky.

Unified Astronomy Thesaurus concepts: Radio astronomy (1338); Millimeter astronomy (1061); Spectral index (1553); Submillimeter astronomy (1647); Transient sources (1851); Core-collapse supernovae (304); Supernovae (1668); Shocks (2086)

1. Introduction

In a cosmic explosion, high-velocity material shocks the ambient medium, accelerating electrons to relativistic speeds and producing synchrotron radiation. Centimeter-wavelength observations have been widely used to model the forward-shock properties from a variety of energetic phenomena, including supernovae (SNe; e.g., Chevalier 1998; Kulkarni et al. 1998; Bietenholz et al. 2021), gamma-ray bursts (GRBs; Chandra & Frail 2012), and tidal disruption events (TDEs; Alexander et al. 2020). Observations at millimeter wavelengths have been less common for both technical and astrophysical reasons: Previous generations of millimeter telescopes had low sensitivity, and mm emission from cosmic explosions tends to be shorter lived than emission at cm wavelengths.

The landscape has changed due to the enhanced sensitivity of mm telescopes and the routine discovery of young

explosions by high-cadence optical surveys. Rapid millimeter follow-up observations of GRBs and SNe is enabling modeling of the reverse shock (Laskar et al. 2018) and the innermost circumstellar medium in massive stars (Maeda et al. 2021). Surprisingly, the nearby ($z = 0.014$) fast optical transient AT 2018cow (Prentice et al. 2018; Perley et al. 2019) had luminous millimeter emission that persisted for weeks (Ho et al. 2019b), significantly exceeding expectations from the model used to describe the late-time ($\Delta t \gtrsim 80$ days), low-frequency ($\nu \lesssim 40$ GHz) data (Margutti et al. 2019). Margutti et al. (2019) suggested that the unusual mm emission could arise from a distinct component such as a reverse shock. Ho et al. (2019b) suggested that the millimeter emission was produced while the shock was in a dense confined region and that it abruptly diminished when the shock passed into lower-density material.

Here we present millimeter, radio, and X-ray observations of ZTF 20acigmel (AT 2020xnd), which appears to be a distant ($z = 0.2433$) analog to AT 2018cow. The optical light curves and spectra of AT 2020xnd were published in Perley et al. (2021). In short, AT 2020xnd was discovered on 2020 October 12 by the Zwicky Transient Facility (Bellm et al. 2019; Graham et al. 2019) and flagged by filters designed to find optical transients that are evolving faster than ordinary SNe (Ho et al.

¹³ NASA Einstein Fellow.



2020a; Perley et al. 2021). More precisely, the optical lightcurve of AT 2020xnd had a duration above half-maximum of $t_{1/2} = 3\text{--}5$ days (Perley et al. 2021), similar to the $t_{1/2} \sim 3$ day duration of the optical light curves of AT 2018cow (Margutti et al. 2019; Perley et al. 2019) and ZTF 18abvkwla (AT 2018lug; Ho et al. 2020b), and much faster than the $t_{1/2} \gtrsim 10$ days of ordinary SNe (Perley et al. 2020a; Ho et al. 2021). Our observations represent only the second mm observations of an AT 2018cow analog. As was the case for AT 2018cow, we find that the early-time millimeter-wavelength data are difficult to reconcile with the late-time centimeter-wavelength data.

The paper is organized as follows. In Section 2 we describe observations from the Northern Extended Millimeter Array (NOEMA), the Australia Telescope Compact Array (ATCA; Frater et al. 1992), the Submillimeter Array (SMA; Ho et al. 2004), the Very Large Array (VLA; Perley et al. 2011), and the Chandra X-ray Observatory (Chandra). We model the forward shock in Section 3 and explore several possible origins for the millimeter-wavelength emission. We conclude that the most likely explanation is synchrotron radiation from a thermal electron-energy distribution (relativistic Maxwellian). In Section 4 we discuss the origin of the X-ray emission. In Section 5 we estimate the detection rates of events like AT 2018cow and AT 2020xnd in current and upcoming millimeter and radio time-domain surveys.

Throughout this paper we use MJD 59,132.0 (2020 October 10.0) as the reference epoch t_0 , following Perley et al. (2021). We assume a flat Λ CDM cosmology with $H_0 = 67.7 \text{ km s}^{-1} \text{ Mpc}^{-1}$ and $\Omega_M = 0.307$ (Planck Collaboration et al. 2016), implying a luminosity distance to the source of 1261 Mpc and an angular-diameter distance of 816 Mpc. Additional submillimeter and radio observations were obtained by an independent observing team and are presented and interpreted in Bright et al. (2022).

2. Observations

In this section we present the millimeter, radio, and X-ray observations of AT 2020xnd. We compare the observational properties to established classes of core-collapse SNe, as well as to the other “AT 2018cow-like” events: AT 2018cow itself (Margutti et al. 2019; Ho et al. 2019b; Nayana & Chandra 2021), CSS 161010 (Coppejans et al. 2020), and AT 2018lug (Ho et al. 2020b).

Following the identification of AT 2020xnd as a fast and luminous transient (Perley et al. 2020b), we triggered follow-up observations with the VLA. Our first VLA observation began on 2020 October 22.99 UTC, at the X band (8–12 GHz). We detected faint but significant ($24 \pm 6 \mu\text{Jy}$) radio emission consistent with the position of the optical transient (Ho et al. 2020c). The position of the radio source in our brightest X-band observation (on December 20), measured with a Gaussian fit, is $\alpha(\text{J2000}) = 22^{\text{h}}20^{\text{m}}02^{\text{s}}.04$, $\delta(\text{J2000}) = -02^{\circ}50'25''.4$. The observation was taken in A configuration, and the statistical uncertainty on the position is $0''.008$. The uncertainty on the position is dominated by a systematic uncertainty of $0''.02$, calculated as 10% of the FWHM of the synthesized beam¹⁴ at the X band in A configuration.

The detection of radio emission similar in luminosity to that of AT 2018cow motivated us to trigger other facilities. A full description of our radio and millimeter observations and data reduction can be found in Appendix A, and the light curves are shown in Figure 1. We obtained Director’s Discretionary Time with the ATCA at 34 GHz to see whether (like AT 2018cow) the emission was optically thick at these frequencies. We triggered our SMA ToO program¹⁵ and obtained Director’s Discretionary Time with NOEMA to observe at 3 mm, 2 mm, and 1.3 mm.¹⁶ We obtained several more epochs of VLA data¹⁷ from 2020 October–2021 May, spanning the C band (4–8 GHz) to the Q band (40–50 GHz).

As shown in Figure 1, the lightcurve at most frequencies rises as $f_\nu \propto t^2$ before the peak and fades as $F_\nu \propto t^{-4}$. The rise at our lowest frequencies appears shallower, $f_\nu \propto t^1$. A rise of $f_\nu \propto t^2$ was also observed at optically thick frequencies in AT 2018cow (Margutti et al. 2019; Ho et al. 2019b) and interpreted as a constant-velocity shock. Steeply declining radio light curves have been observed in all AT 2018cow-like events at frequencies $\lesssim 10$ GHz (Coppejans et al. 2020; Ho et al. 2020b). From Figure 1 it is clear that the steep decline is chromatic, beginning at later times at lower frequencies. We discuss the origin of the chromatic steep decline in Section 3.

After AT 2018cow itself, our NOEMA observations represent only the second detection of an AT 2018cow-like transient at millimeter wavelengths. The peak flux density of $1.08 \pm 0.05 \text{ mJy}$ at 79 GHz (100 GHz in the rest frame) corresponds to a spectral luminosity of $L_{79 \text{ GHz}} = (2.05 \pm 0.09) \times 10^{30} \text{ erg s}^{-1} \text{ Hz}^{-1}$. As shown in Figure 2, the only transients in the literature with a higher luminosity at similar frequencies are relativistic explosions: long-duration GRBs (e.g., $10^{31} \text{ erg s}^{-1} \text{ Hz}^{-1}$ for GRB 130427A; Perley et al. 2014) and tidal disruption events ($7 \times 10^{31} \text{ erg s}^{-1} \text{ Hz}^{-1}$ for J1644+57; Zauderer et al. 2011). However, the lightcurve of AT 2020xnd rises to peak over a month instead of a few days. In Section 5 we use the 100 GHz lightcurve to estimate the detection rate for events like AT 2020xnd in millimeter transient surveys.

The 10 GHz lightcurve peaks at $f_\nu = 0.180 \pm 0.023 \text{ mJy}$, or $L_{10 \text{ GHz}} = (3.4 \pm 0.4) \times 10^{29} \text{ erg s}^{-1} \text{ Hz}^{-1}$. The time to peak of $t_{\text{pk}} \approx 60$ days is common for centimeter-wavelength emission from core-collapse SNe (Bietenholz et al. 2021), but the luminosity is significantly greater. The luminosity and time-scale are similar to what was observed for AT 2018cow (Margutti et al. 2019; Ho et al. 2019b), CSS 161010 (Coppejans et al. 2020), and AT 2018lug (Ho et al. 2020b).

In Figures 3 and 4 we show the radio–millimeter spectral energy distribution (SED) as a function of time. We regard data obtained within $\Delta t/10$ days as coeval, where Δt is the time since t_0 (defined in Section 1). Based on these observations, we are motivated to consider the evolution of AT 2020xnd in two stages (Section 3). Before $\Delta t = 40$ days, the spectral index from 79 to 94 GHz is relatively flat and does not change with time, even while the overall flux density changes. At 46 days we observe a steep spectral index across the NOEMA bands: a fit to the five high-frequency points gives $\beta = -2.00 \pm 0.23$, where $f_\nu \propto \nu^\beta$. After $\Delta t = 70$ days, the SED cascades down in flux and frequency: The bulk of the radiation emerges at successively lower frequencies, with the peak luminosity also decreasing.

¹⁴ <https://science.nrao.edu/facilities/vla/docs/manuals/oss/performance/positional-accuracy>

¹⁵ Program 2020A-S037; P.I. Ho.

¹⁶ Program D20AF and D20AG; P.I. Ho.

¹⁷ Program VLA/20A-374 and Program VLA/20B-205; P.I. Ho.

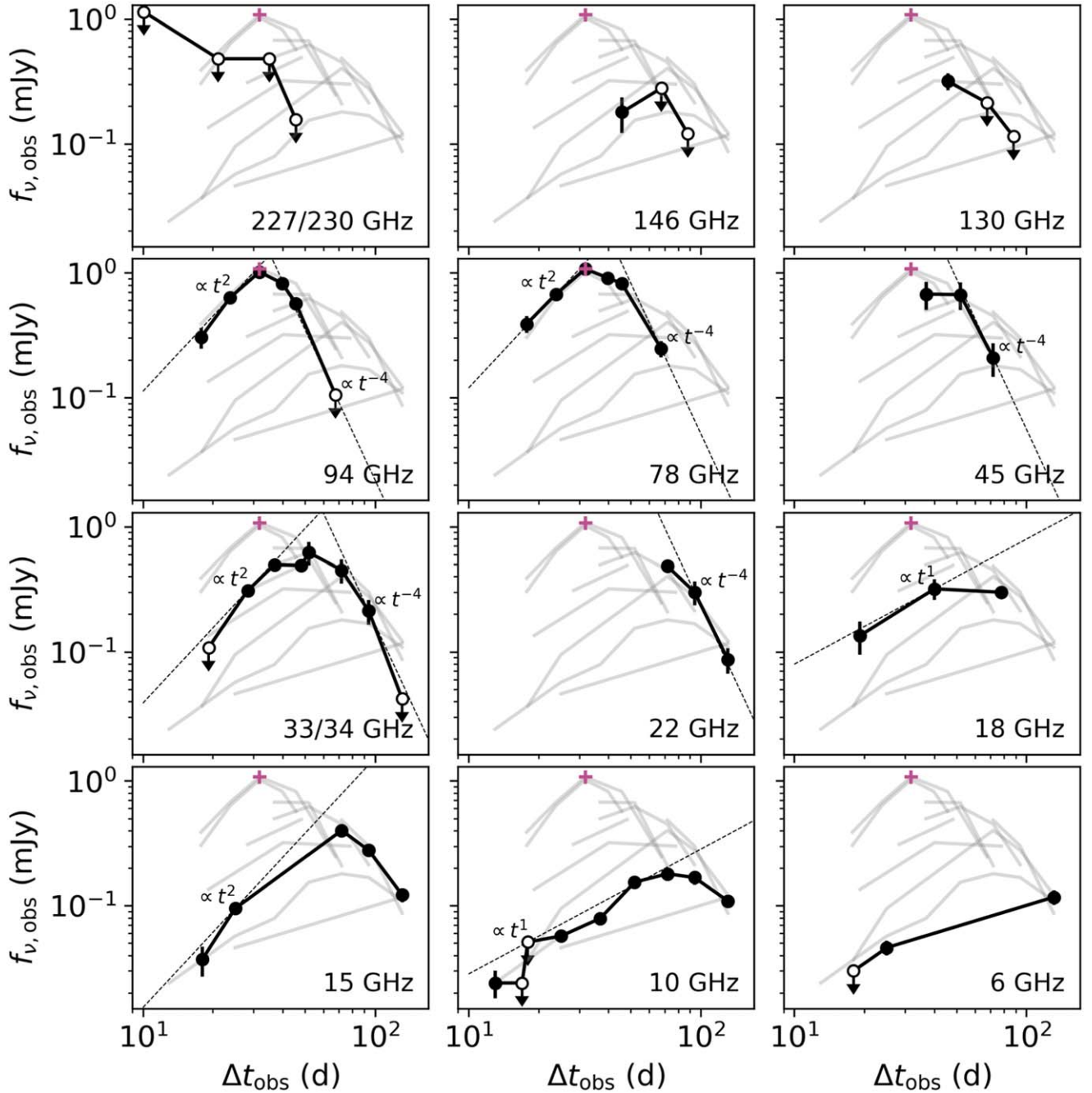


Figure 1. Millimeter and radio light curves of AT 2020xnd from NOEMA, the ATCA, and the VLA. We include all frequencies that have two or more observations. The red cross marks the peak of the 79 GHz NOEMA lightcurve, which was 1.1 mJy at 32 days. The full set of light curves is shown as gray lines in the background, and each panel highlights an individual observing band in black. Open circles represent 3σ upper limits. No cosmological correction has been applied, and time is in the observer frame.

In addition to radio and millimeter observations, AT 2020xnd was observed over $\Delta t = 20$ –150 days with Chandra (Matthews et al. 2020). We retrieved the observations from the Chandra data archive and analyzed them with the procedure described in Appendix B. The lightcurve is shown in Figure 5. The peak luminosity of $7 \times 10^{42} \text{ erg s}^{-1}$ (observer frame) is almost identical to that of AT 2018cow at the same epoch (Rivera Sandoval et al. 2018; Kuin et al. 2019; Margutti et al. 2019; Ho et al. 2019b). CSS 161010 was also detected in X-rays but only at $\Delta t > 100$ days (Coppejans et al. 2020).

3. Analysis

In Section 2 we presented millimeter, radio, and X-ray observations of AT 2020xnd. In this section we use the data to derive basic properties of the forward shock. We consider the origin of the X-rays separately (Section 4). As discussed in Section 2, the evolution of AT 2020xnd appears to proceed in two stages: an early stage ($\Delta t < 40$ days) when the spectral index from 79 to 94 GHz is relatively flat and unchanging and a later stage ($\Delta t > 70$ days) when the SED clearly cascades down both in flux and frequency. We begin by considering the later

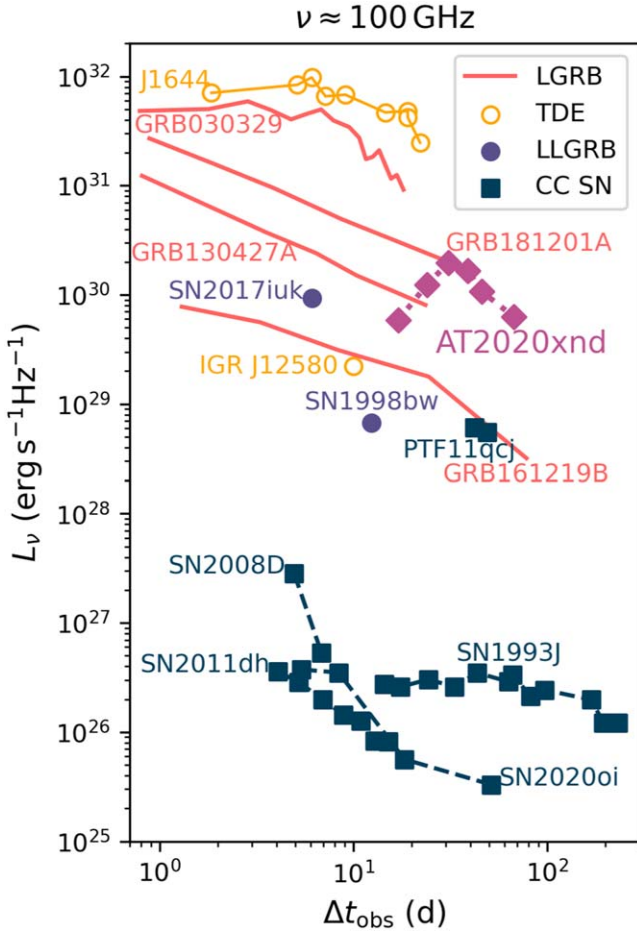


Figure 2. The NOEMA 94 GHz lightcurve of AT 2020xnd compared to light curves of millimeter-bright cosmic explosions at similar frequencies: long-duration gamma-ray bursts (LGRBs), tidal disruption events (TDEs), low-luminosity GRBs (LLGRBs), and core-collapse (CC) SNe. Data obtained from Kulkarni et al. (1998), Sheth et al. (2003), Weiler et al. (2007), Soderberg et al. (2010), Zauderer et al. (2011), Horesh et al. (2013), Corsi et al. (2014), Perley et al. (2014), Yuan et al. (2016), Perley et al. (2017), Laskar et al. (2018, 2019), and Maeda et al. (2021). All observations are in the observer frame.

stage, because the behavior is similar to what has been seen in previous events.

3.1. Late Stage ($\Delta t > 70$ days)

To model the late-time centimeter-wavelength data, we follow the standard approach for nonrelativistic SNe (Chevalier 1998; Kulkarni et al. 1998; Soderberg et al. 2005). We assume that the SEDs arise from synchrotron self-absorption of nonthermal electrons shock-accelerated into a power-law energy distribution of index $p = 3$ down to a minimum Lorentz factor γ_m . The same framework has been applied to AT 2018cow and analogs to find shock speeds ranging from $v = 0.1c$ (AT 2018cow; Margutti et al. 2019; Ho et al. 2019b) to $v = 0.6c$ (CSS 161010; Coppejans et al. 2020). We apply a basic cosmological correction to the flux-density measurements by dividing the observed values by a factor of $(1+z)$.

The assumptions behind this framework are summarized in Appendix C. We note that the standard equations in the literature (Chevalier 1998) assume that the synchrotron self-absorption (SSA) frequency is below the cooling frequency, $\nu_a < \nu_c$. This is not necessarily valid: for AT 2018cow, $\nu_a > \nu_c$ at early times (Ho et al. 2019b), as a consequence of a large

amount of energy being injected into a small volume of material, a regime selectively probed by high-frequency observations. In Appendix C we provide the corrected equations for the regime of $\nu_a > \nu_c$.

We model the SED as a broken power law. Following Granot & Sari (2002), we have

$$f_\nu = f_p \left[\left(\frac{\nu}{\nu_p} \right)^{-s\beta_1} + \left(\frac{\nu}{\nu_p} \right)^{-s\beta_2} \right]^{-1/s}, \quad (1)$$

where f_p and ν_p are the peak flux and peak frequency, respectively, β_1 and β_2 are the spectral indices on either side of the break, and s is a smoothing parameter. We further assume that the peak flux and peak frequency evolve as power laws in time, with $f_p \propto t^{\alpha_1}$ and $\nu_p \propto t^{\alpha_2}$. We begin by assuming that the peak is governed by SSA with an optically thick spectral index $\beta_1 = 5/2$ (Rybicki & Lightman 1986) and optically thin spectral index $\beta_2 = -1$, where $\beta_2 = -(p-1)/2$ in the slow-cooling regime $\nu < \nu_c$. We assume $p = 3$.

For the fit, we must consider the effects of scintillation. Radio point sources can exhibit significant variability in their centimeter-wavelength light curves due to inhomogeneities in the interstellar medium (Rickett 1990; Narayan 1992; Walker 1998). The light curves and SEDs of AT 2020xnd are fairly smooth (Section 2), with the possible exception of the early-time 10 GHz lightcurve (Figure 1) and the 6 GHz flux-density values in the SEDs (Figure 3).

The NE2001 model (Cordes & Lazio 2002) predicts that the transition frequency in the direction of AT 2020xnd is 9 GHz and that the maximum source size subject to scintillation is $3\text{--}4 \mu\text{as}$ (Walker 1998). Later in this section, we find $R \approx 3 \times 10^{16} \text{ cm}$ at these epochs, which corresponds to $\theta \approx 2 \mu\text{as}$. So, we conclude that observations with $\nu_{\text{obs}} \lesssim 9 \text{ GHz}$ could be affected by scintillation; at the transition frequency, variations could be of order unity. We therefore leave out the 6 GHz data points in our fitting.

The resulting fit is shown in the left panel of Figure 6. Using `curve_fit` in `scipy`, we find that $f_p = 0.68 \pm 0.08 \text{ mJy}$ and $\nu_p = 22 \pm 1 \text{ GHz}$ at 58 days in the rest frame, $\alpha_1 = -2.2 \pm 0.1$, $\alpha_2 = -0.88 \pm 0.20$, and $s = 1.0 \pm 0.2$. The reduced $\chi^2 = 1.1$ with $N = 8$ degrees of freedom. The corresponding forward-shock properties (using Equations (C5) and (C6) in Appendix C) are $R \approx 2 \times 10^{16} \text{ cm}$ and $B \approx 0.9 \text{ G}$, with $R \propto t^{-0.2}$ and $B \propto t^{-0.7}$. The magnetic field strength is close to what was observed for SN 2003L (Soderberg et al. 2005) and SN 2003bg (Soderberg et al. 2006a).

The constant or even decreasing radius we inferred above is not consistent with our assumption of an outwardly propagating shock. So, we fit the same data fixing the shock speed to be constant (a near-constant shock speed was observed in AT 2018cow; Margutti et al. 2019; Ho et al. 2019b; Nayana & Chandra 2021). The results are shown in the right panel of Figure 6. We find $f_p = 0.83 \pm 0.11$, $\nu_p = 23 \pm 1$, $\alpha_1 = -2.1 \pm 0.1$, and $s = 0.78 \pm 0.13$. The reduced $\chi^2 = 2.8$ with $N = 9$ degrees of freedom. The magnetic field strength goes as $B \propto t^{-1.8}$. This solution is also not physical: The corresponding density profile is $n_e \propto B^2 \propto t^{-3.6} \propto R^{-3.6}$, and the standard model does not apply to such a steep density profile ($k \geq 3$, where $\rho \propto r^{-k}$).

Allowing the shock to be mildly decelerating (e.g., $R \propto t^{0.8}$, the value observed in CSS 161010; Coppejans et al. 2020) results in a shallower density profile. We can estimate the

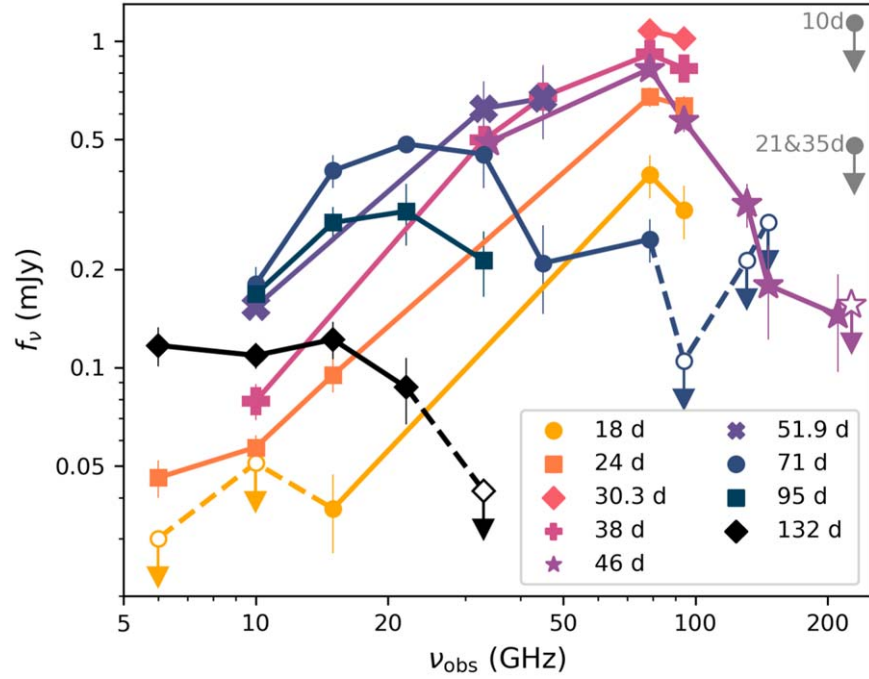


Figure 3. The evolution of the millimeter and radio spectral energy distribution of AT 2020xnd. Observations are considered coeval if they are within $\Delta t/10$ days of each other. SMA 230 GHz upper limits are shown in gray. At other epochs, upper limits are indicated with empty symbols and connected with dashed lines. Observations are in the observer frame.

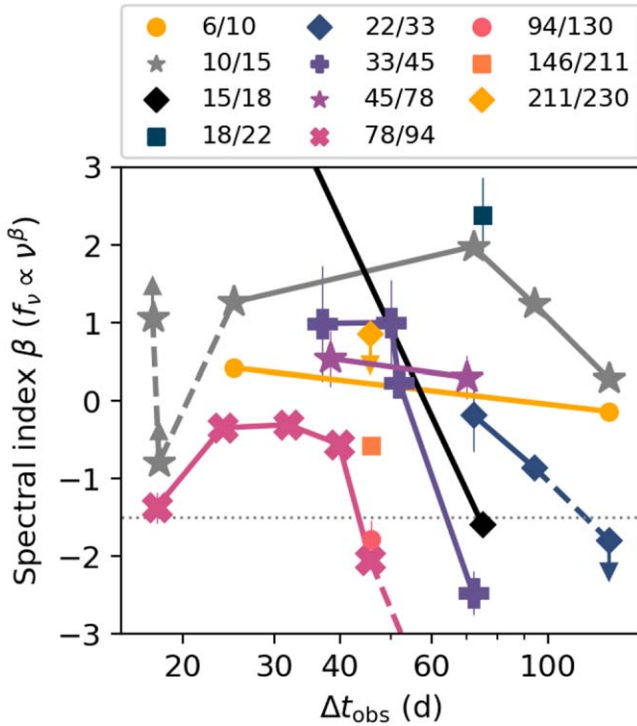


Figure 4. The evolution of the spectral index β over time, where $f_\nu \propto \nu^\beta$. The spectral index is measured between adjacent frequency bands at every coeval epoch Δt , defined as epochs where the observations take place within $\Delta t/10$ days of each other. Epoch and frequencies are reported in the observer frame. The horizontal dotted line indicates $\beta = -1.5$, which might be expected from an electron-energy distribution of $p = 3$ in the fast-cooling regime. For clarity, we do not show one 130/146 GHz point ($\beta \approx -5$), one 15/18 GHz point ($\beta \approx 7$), and one 78/94 point ($\beta \approx -5$).

density profile for different rates of shock deceleration using the peak flux density of the lightcurve at each observing frequency, shown in Figure 7. Including only points below

90 GHz, we find $f_p \propto \nu_p^{1.0 \pm 0.1}$. Combining Equations (C14) and (C15), for this value of $d \ln(f_p)/d \ln(\nu_p)$ we find

$$k = \frac{-20 + 54\alpha_r}{10\alpha_r}, \quad (2)$$

where α_r is defined as $R \propto t^{-\alpha_r}$. So, a constant-velocity shock $\alpha_r = 1$ corresponds to $k = 3.4$, while a mildly decelerating shock $\alpha_r = 0.8$ corresponds to $k = 2.9$. For a wind profile $k = 2$ we would require $\alpha_r = 0.6$. In summary, we cannot robustly constrain the hydrodynamics of the shock using our late-time VLA data alone. However, under the reasonable physical assumption of a mildly decelerating shock, the data could be explained by a medium with a steep density profile.

We can use our single-epoch estimates of R and B at 71 days in the observer frame (58 days in the rest frame) to estimate the mean velocity of the shock v , the total thermalized energy U , and the ambient density n_e . Following the standard approach to modeling radio SNe (Kulkarni et al. 1998; Soderberg et al. 2005, 2006b; Chevalier & Fransson 2006; Soderberg et al. 2010; Horesh et al. 2013), we assume equipartition, $\epsilon_e = \epsilon_B = 1/3$. We find that the mean velocity $v \approx 0.15c$: like the other AT 2018cow analogs, fast but subrelativistic. From Equation (12)¹⁸ in Ho et al. (2019b), we have

$$U = \frac{1}{\epsilon_B} \frac{4\pi}{3} R^3 \frac{B^2}{8\pi} \approx 2 \times 10^{48} \text{ erg}. \quad (3)$$

This is very similar to the value of U found for AT 2018cow at $\Delta t = 22$ days. As shown in Figure 8, AT 2018cow and its analogs have very high measured energies compared to other subrelativistic cosmic explosions, with the exception of FIRST J1419 (Law et al. 2018; Mooley et al. 2022) and VT 1210+5946 (Dong et al. 2021).

¹⁸ We do not include a filling factor here.

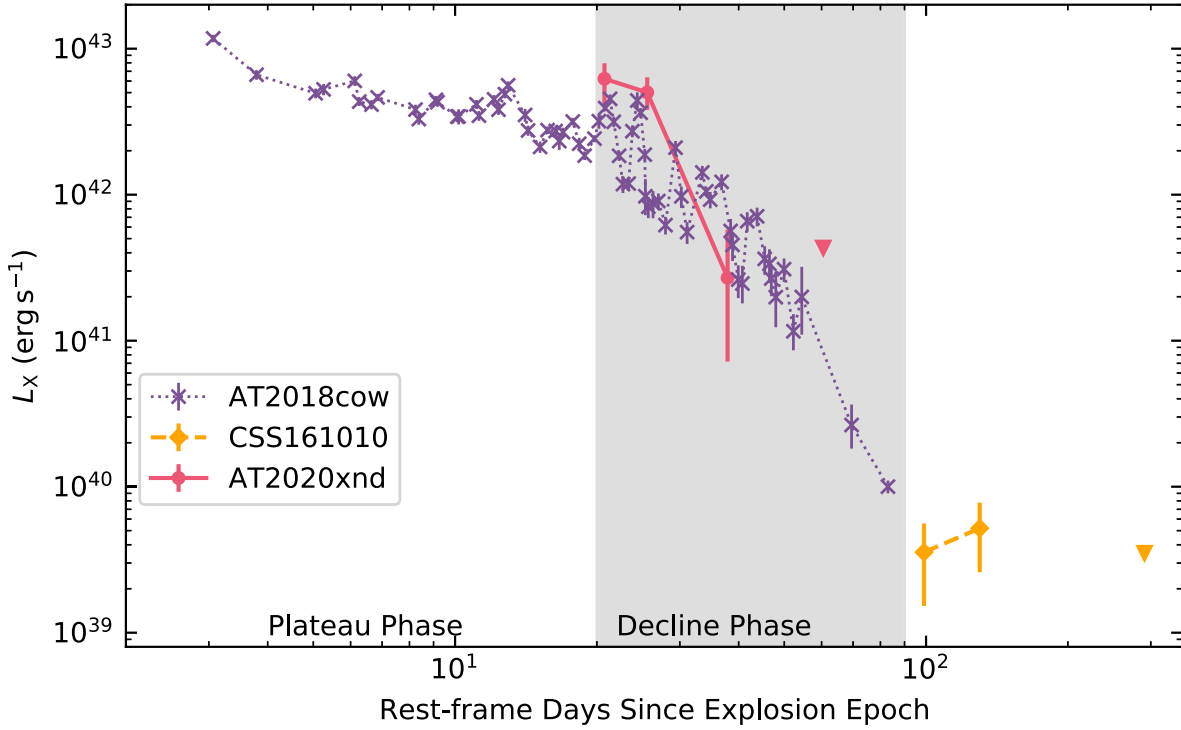


Figure 5. The 0.3–10 keV X-ray lightcurve of AT 2020xnd from Chandra compared to the 0.3–10 keV X-ray light curves of AT 2018cow (Rivera Sandoval et al. 2018; Kuin et al. 2019; Margutti et al. 2019; Ho et al. 2019b) and CSS 161010 (Coppejans et al. 2020). The gray shaded region marks the “decline phase” delineated in Ho et al. (2019b). The luminosity of AT 2020xnd is similar to that of AT 2018cow at the same phase, and we see tentative evidence of the same steep decline, although the data are significantly more sparse. Note that the AT 2020xnd observations have not been K -corrected.

To estimate the ambient density, we assume that the number densities of protons and electrons are equal ($n_e = n_p$) and that the medium is composed of fully ionized hydrogen, so that $n_e = \rho/(\mu_p m_p)$, where $\mu_p = 1$. We therefore have

$$n_e = \frac{B^2}{16\pi\epsilon_B m_p v^2} \approx 4 \times 10^3 \text{ cm}^{-3}. \quad (4)$$

At a similar epoch (70 days), an ambient density of $n_e = 50 \text{ cm}^{-3}$ was inferred for CSS161010.

Assuming a steady wind, we can convert the ambient density to a mass-loss rate \dot{M} , where

$$\dot{M} = n_e 4\pi m_p r^2 v_w, \quad (5)$$

and v_w is the velocity of the wind. Taking $v_w = 1000 \text{ km s}^{-1}$ we have $\dot{M} \approx 2 \times 10^{-4} M_\odot \text{ yr}^{-1}$, while for 10 km s^{-1} we have $2 \times 10^{-6} M_\odot \text{ yr}^{-1}$. The inferred velocity and \dot{M} are shown in Figure 9 compared to other energetic explosions.

We can use the shock speed to estimate the minimum Lorentz factor of the electrons γ_m ,

$$\gamma_m = 1 + \frac{1}{2} \left(\frac{p-2}{p-1} \right) \epsilon_e \frac{m_p}{m_e} \frac{v^2}{c^2} \approx 4. \quad (6)$$

From γ_m we can estimate the characteristic synchrotron frequency ν_m , the frequency of electrons whose Lorentz factor is γ_m :

$$\nu_m = \gamma_m^2 \nu_g, \quad (7)$$

where

$$\nu_g = \frac{eB}{2\pi m_e c}, \quad (8)$$

We find $\nu_m \approx 0.05 \text{ GHz}$, which is below our observing frequencies. Finally, we can estimate the cooling frequency ν_c , where

$$\nu_c = \gamma_c^2 \nu_g \quad (9)$$

and

$$\gamma_c = \frac{6\pi m_e c}{\sigma_T B^2 t}. \quad (10)$$

We find $\nu_c = 100 \text{ GHz}$, significantly above the VLA frequencies, and consistent with our assumption that $\nu_a < \nu_c$ at late times. The forward-shock properties at 71 days in the observer frame are summarized in Table 1.

3.2. Early Stage

In Section 3.1 we modeled the late-time low-frequency emission assuming a power-law distribution of electrons and a radio SED governed by SSA, a standard approach to modeling radio SNe that has been applied to AT 2018cow (Margutti et al. 2019; Ho et al. 2019b), AT 2018lug (Ho et al. 2020b), and CSS 161010 (Coppejans et al. 2020). For both AT 2018cow and AT 2020xnd, however, the SSA model derived from low-frequency late-time observations is not consistent with the early millimeter-wave observations. Margutti et al. (2019) suggested that the early millimeter emission might arise from a separate component such as a reverse shock, and Ho et al. (2019b) suggested that during the millimeter-bright phase the shock was passing through higher-density material that terminated abruptly, resulting in a rapid decay in both flux and frequency. In this section we consider several possibilities for the origin of the high-frequency emission from AT 2020xnd

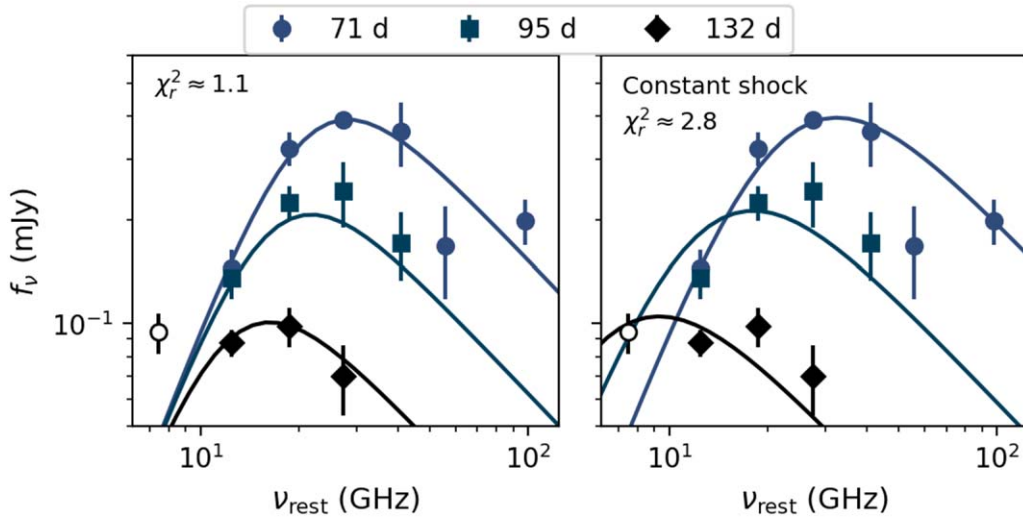


Figure 6. Broken power-law fit to the late-time data. Each color/symbol combination corresponds to a different observer-frame epoch, the same as in Figure 3. The single point below 9 GHz is excluded from the fit due to possible scintillation, indicated with an unfilled circle. We assume that the peak flux and peak frequency also evolve as a power law in time, that the optically thick spectral index is $\beta = 5/2$, and that the optically thin spectral index is $\beta = -1$, where $f_\nu \propto \nu^\beta$. For the fit shown in the right-hand panel, we also assume that the shock speed is constant, $R \propto t$. The flux-density values have a basic cosmological correction applied, and frequency values are reported in the rest frame.

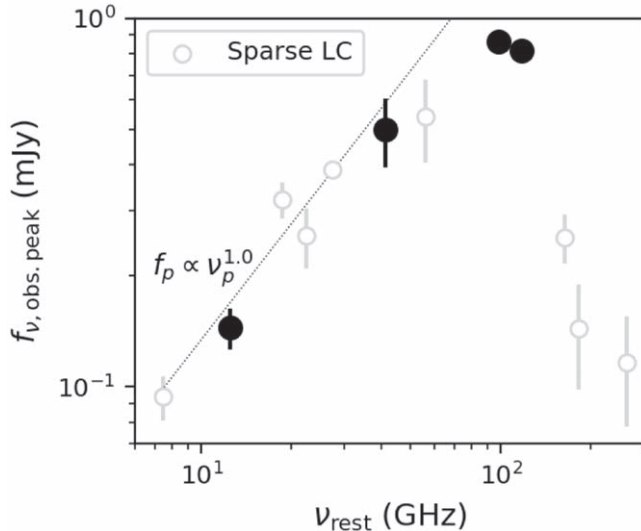


Figure 7. The peak observed flux density of the lightcurve at different frequencies. Filled points are from frequencies with a well-sampled lightcurve peak (94, 79, 33, and 10 GHz). Empty points are from light curves that do not have a well-sampled peak.

observed with NOEMA at $\Delta t < 50$ days: continuous shock acceleration with a nonthermal (Section 3.2.1) or thermal (Section 3.2.2) electron-energy distribution and nonsteady-state particle injection (Section 3.2.3).

3.2.1. Continuous Shock Acceleration + SSA + Power-law Electron-energy Distribution

First, we apply the same framework used to model the late-time low-frequency data in Section 3.1: continuous shock acceleration resulting in the acceleration of electrons into a power-law energy distribution, with the peak in the SED governed by SSA. We find that a power-law evolution in the peak flux and frequency does not do a good job of describing the data. So, we treat each epoch of 79 + 94 GHz data independently, fixing $\beta_1 = 5/2$ and $\beta_2 = -1.5$ or $\beta_2 = -1$

(depending on whether we find the SED to be in the slow- or fast-cooling regime). The fits are shown in Figure 10, and the corresponding physical parameters are listed in Table 2. We caution that only epochs 38 days and 46 days have reasonably well-sampled SEDs; the other fits should be regarded as lower limits on the peak frequency. If the optically thick spectral index is shallower (as appears to be the case), the peak would be at a higher frequency and the inferred radius and velocity would be lower. In Table 2 we also provide a limit based on $\nu_p \lesssim 100$ GHz.

With our sparsely sampled SEDs, we cannot precisely measure the physical properties of the forward shock from our early observations. However, particularly from the observations at 38 days and 46 days, it appears that the density is an order of magnitude higher than at 71 days, consistent with our inference in Section 3.1 of a steep $n_e \propto r^{-3}$ density profile. The shock speed of $v \approx 0.2$ is similar to our measurement at 71 days. We conclude that if the framework presented in this section is correct, then the shock likely propagated through a particularly high-density region, and that the density began decreasing abruptly as $n_e \propto r^{-3}$ at $\Delta t \approx 50$ –60 days. This is very similar to the conclusion drawn from the 230 GHz lightcurve of AT 2018cow, which plateaued for ≈ 50 days before abruptly declining (Ho et al. 2019b). A density profile steeper than a steady wind was inferred for CSS 161010 (Coppejans et al. 2020), and—as discussed for that object—implies nonsteady mass loss (Smith 2014).

3.2.2. Continuous Shock Acceleration + SSA + Thermal Electron-energy Distribution

In Section 3.2.1 we modeled the early high-frequency emission with the same framework used to model the late-time low-frequency emission in Section 3.1. We found that at early times the shock likely propagated through a region of high density ($\approx 10^4 \text{ cm}^{-3}$) and that the density decreased abruptly after 50 days. In this section we consider the possibility that, instead, the assumption of all electrons being accelerated into a power-law distribution is incorrect: that there was a significant

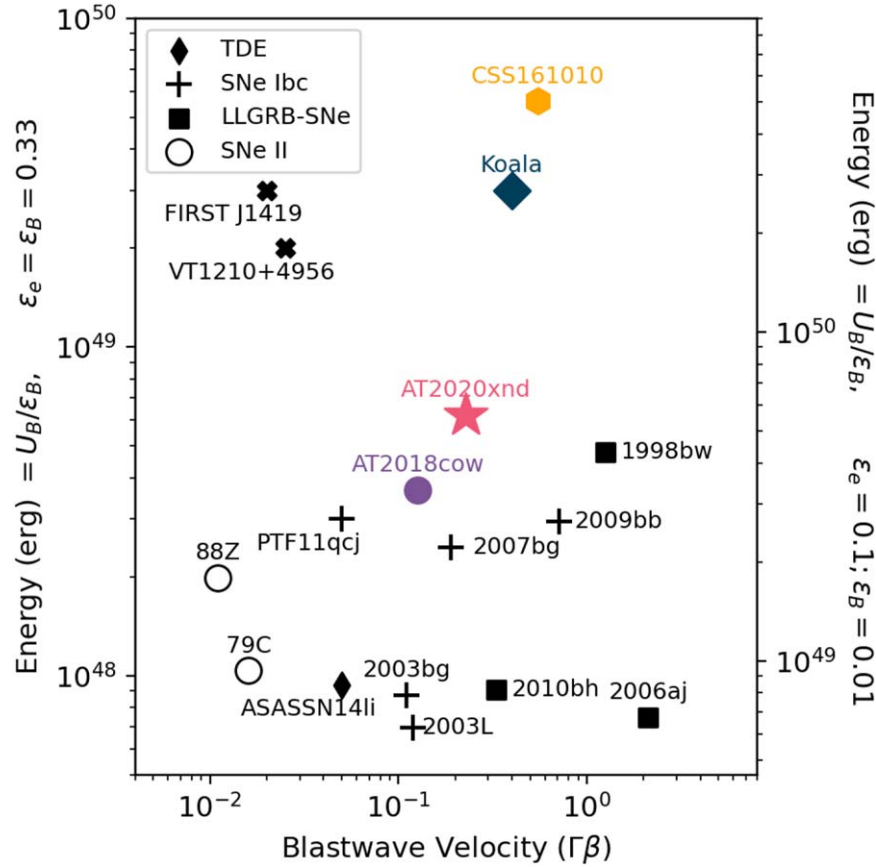


Figure 8. AT 2020xnd (star) in velocity–energy space compared to other classes of radio-luminous transients: TDEs (filled diamonds; Alexander et al. 2016), Ibc SNe (crosses; Corsi et al. 2014; Soderberg et al. 2005, 2006a, 2010; Salas et al. 2013), SNe associated with LLGRBs (filled squares; Kulkarni et al. 1998; Soderberg et al. 2006c; Margutti et al. 2013), Type II SNe (open circles; van Dyk et al. 1993; Weiler et al. 1986, 1991), and two luminous radio transients identified in radio survey data (filled X; Law et al. 2018; Dong et al. 2021; Mooley et al. 2022). For reference, GRBs lie above the plot at $10^{50} \text{ erg} < U < 10^{52} \text{ erg}$, and the relativistic TDE Swift J1644+57 (Zauderer et al. 2011; Berger et al. 2012; Eftekhari et al. 2018) lies at 10^{51} erg in this framework. Transients similar to AT 2018cow are shown as colored points: CSS 161010 (Coppejans et al. 2020), AT 2018lug (the “Koala”; Ho et al. 2020b), and AT 2018cow (Margutti et al. 2019; Ho et al. 2019b). For more details see Appendix C in Ho et al. (2019b).

population of electrons remaining in a thermal distribution, i.e., a relativistic Maxwellian.

Our primary motivation for considering a thermal population is the steep spectral index observed at 46 days. From five NOEMA data points, we measure $\beta = -2.0 \pm 0.2$, which corresponds to $p = 4.0 \pm 0.5$ in the fast-cooling regime. In the test-particle limit, diffuse shock acceleration predicts $p = 2$ for nonrelativistic shocks (e.g., Blandford & Eichler 1987). Radio SNe are often inferred to have steeper electron power-law indices ($p = 3$; e.g., Soderberg et al. 2005). Deviations from $p = 2$ may be expected from nonlinear effects (departure from the test-particle approximation). For example, Caprioli et al. (2020) recently suggested that self-generated Alfvén waves downstream of the shock can enhance particle advective losses and thus steepen the spectrum.

However, to our knowledge, inferred values as steep as $p = 3.5\text{--}4$ are unusual. Reviewing the literature, we identified only a handful of events with measured values of $p \geq 3.5$. One is AT 2018cow itself: At $\Delta t = 10$ days the spectral index across the SMA observing bands was $\beta = -1.86 \pm 0.03$, or $p = 3.72 \pm 0.06$ in the fast-cooling regime. Another is CSS 161010: at $\Delta t = 99$ days, Coppejans et al. (2020) measure $p = 3.5^{+0.4}_{-0.1}$. Finally, the ultralong GRB 130925A (Horesh et al. 2015) had $\beta_2 = 1.4 \pm 0.1$, corresponding to $p = 3.8 \pm 0.2$.

Horesh et al. (2015) argued that the steep frequency cutoff observed in GRB 130925A could reflect an underlying steep cutoff in the electron-energy distribution and that a monoenergetic distribution was a better match to the data. Here we consider whether a Maxwellian energy distribution (Eichler & Granot 2006) could explain the SED of AT 2020xnd, which is physically better motivated than a monoenergetic distribution, as well as the other events with steep spectra (Figure 11). Interestingly, we note that CSS 161010 had an observed optically thick power-law index of $f_\nu \propto \nu^2$, which is an expectation of a thermal rather than nonthermal electron distribution.

The effect of having a thermal electron population in addition to a power-law population has been considered by various authors, primarily in the context of light curves and spectra of GRB afterglows (Giannios & Spitkovsky 2009; Ressler & Laskar 2017; Jóhannesson & Björnsson 2018; Warren et al. 2018). In general, the Maxwellian adds an excess of flux close to the characteristic synchrotron frequency of the thermal electrons ν_T (Equation (13), which results in a steeper spectrum above the peak frequency (an exponential) that eventually reconnects to the power law. Over time, the characteristic frequency of this additional component can decrease if the shock decelerates. At $\nu \gg \nu_T$, following Mahadevan et al. (1996), the spectrum takes the form

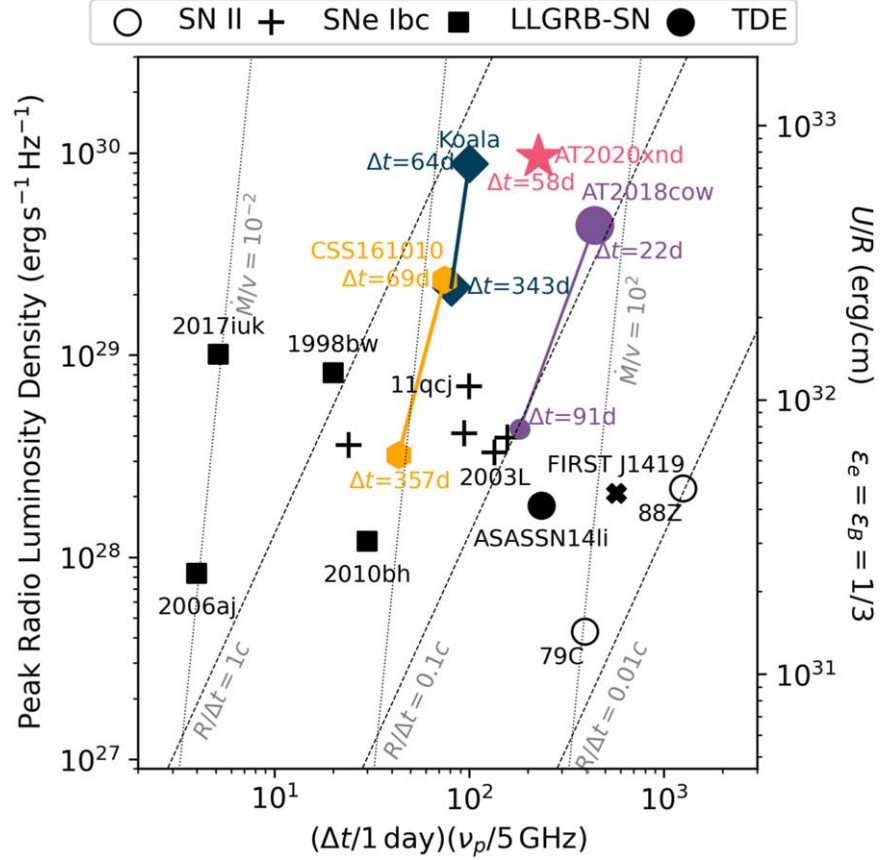


Figure 9. The peak luminosity of AT 2020xnd and other AT 2018cow-like explosions on two different epochs, compared to classes of energetic transients (see Chevalier 1998; Soderberg et al. 2010; Ho et al. 2019b). Lines of constant mass-loss rate (scaled to wind velocity) are shown in units of $10^{-4} M_{\odot} \text{ yr}^{-1}/1000 \text{ km s}^{-1}$. Note that the dotted lines assume that the radio peak is due to synchrotron self-absorption. Values for AT 2020xnd are from this work. Other values are from Ho et al. (2019b, 2020b), Coppejans et al. (2020), Margutti et al. (2019), Corsi et al. (2014), Soderberg et al. (2010), Kulkarni et al. (1998), Soderberg et al. (2006b), Margutti et al. (2013), Horesh et al. (2013), Krauss et al. (2012), Salas et al. (2013), Soderberg et al. (2005, 2006a), van Dyk et al. (1993), and Weiler et al. (1986).

Table 1

Quantities Derived from Measurements on Day 71 (Observer Frame), under the Standard Assumption that the Electron-energy Distribution is a Power Law and that the SED Peak is Governed by Synchrotron Self-absorption

Parameter	Value
$\nu_a = \nu_p$ (GHz)	22 ± 1
$F_{\nu,p}$ (mJy)	0.68 ± 0.08
R (10^{16} cm)	2.2 ± 0.2
B (G)	0.87 ± 0.04
v/c	0.15 ± 0.01
U (10^{48} erg)	2.1 ± 0.5
n_e (10^3 cm^{-3})	3.7 ± 0.6
ν_c (GHz)	100 ± 5

Note. We assume equipartition, $\epsilon_e = \epsilon_B = 1/3$. We provide formal errors from the fit, but caution that the uncertainties on these parameters are dominated by systematics and by our assumptions.

$f_{\nu} \propto \nu e^{-1.8899x^{1/3}}$, where $x = \frac{2\nu}{3\nu_T}$. We use our NOEMA data to analytically estimate ν_T . The local spectral index is $\beta = d \ln f_{\nu} / d \ln \nu \approx 1 - (1/3)1.8899x^{1/3}$. So, $\nu_T \approx (2/3)\nu[3(1 - \beta)/1.8899]^{-3}$. Because the spectral index we measure is close to -2 , we find $\nu_T \approx 0.6$ GHz.

Given that $\nu_T \sim 1$ GHz and that we observe a steep optically thick spectral index from 10 GHz to 100 GHz (instead of the $\nu^{1/3}$ expected for a Maxwellian; Mahadevan et al. 1996), we

conclude that if the emission is from a thermal population, then it must be absorbed: The frequency of the peak of the SED, ν_{peak} , is set by the synchrotron self-absorption frequency, $\nu_{\text{peak}} = \nu_a$. A Maxwellian with synchrotron self-absorption has the form

$$f_{\nu} = f_m \left(\frac{\nu}{\nu_T} \right)^2 \left\{ 1 - \exp \left[-\tau_m \left(\frac{\nu}{\nu_T} \right)^{-1} I \left(\frac{2\nu}{3\nu_T} \right) \right] \right\}, \quad (11)$$

where the function $I(x)$ is given by Mahadevan et al. (1996),

$$I(x) \approx 2.5651 \left(1 + \frac{1.92}{x^{1/3}} + \frac{0.9977}{x^{2/3}} \right) e^{-1.8899x^{1/3}}, \quad (12)$$

f_m is a scaling constant (it is the flux density at frequency ν_T), and τ_m is related to the SSA optical depth at this frequency (up to a factor $I(2/3) \approx 2.2$).

In Figure 11 we show data from AT 2020xnd, AT 2018cow, and CSS 161010, fit with Equation (11) and provide the best-fit parameters in Table 3. A more general treatment of the self-absorbed Maxwellian model is presented in a separate work by Margalit & Quataert (2021). We find that the model describes the data well: in particular, it reproduces the $f_{\nu} \propto \nu^2$ optically thick spectral index observed in CSS 161010 and AT 2018cow, as well as the steep observed optically thin spectral index observed in all three events. For reference, in Figure 11 we also

Table 2

Quantities Derived from Early Epochs that Have 79 GHz + 94 GHz NOEMA Observations, under the Standard Assumption that the SED Peak is Governed by Synchrotron Self-absorption and that the Electrons are Accelerated into a Power-law Energy Distribution

	18 days	24 days	30.3 days	38 days	46 days
$\nu_a = \nu_p$ (GHz)	60–100	50–100	70–100	61.7 ± 1.2	52.6 ± 2.2
$F_{\nu,p}$ (mJy)	0.3–0.6	0.6–1.2	0.9–1.6	1.38 ± 0.04	1.05 ± 0.04
R (10^{16} cm)	0.3–0.8	0.5–1.3	0.6–1.0	1.11 ± 0.03	1.14 ± 0.05
B (G)	2.4–4.3	1.9–4.0	2.6–3.9	2.28 ± 0.04	2.00 ± 0.08
v/c	0.09–0.2	0.09–0.3	0.09–0.2	0.138 ± 0.003	0.119 ± 0.005
U (10^{48} erg)	0.2–0.7	0.4–1.8	0.7–1.8	28.8 ± 1.7	1.5 ± 0.2
n_e (10^3 cm $^{-3}$)	16–270	5.5–200	30–210	19.8 ± 0.4	29.7 ± 3.7
ν_c (GHz)	12–71	9.5–95	6.3–20	31.6 ± 0.8	20.6 ± 0.9

Note. We assume equipartition, $\epsilon_e = \epsilon_B = 1/3$, and $p = 3$. Epochs are listed in the observer frame. Only epochs 38 days and 46 days have well-sampled SEDs. We provide formal uncertainties from our fits but caution that the true uncertainties are dominated by systematics and our assumptions.

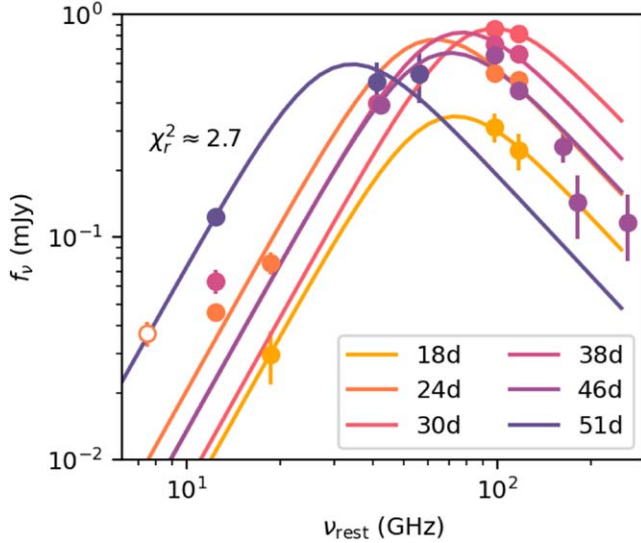


Figure 10. Broken power-law fits to the early-time millimeter and radio data of AT 2020xnd. Each epoch is fit independently. We assume an optically thick spectral index of $\beta = 5/2$, the expectation for synchrotron self-absorption of a nonthermal electron population, although as discussed in the text it is more likely that a thermal electron population contributes significantly to the emission at these stages.

show a power law with $f_\nu \propto \nu^{-1.5}$. The exponential cutoff does a better job of reproducing the data, and we note that such a steep power law would require $p \geq 3$, which is difficult to explain in diffusive-shock-acceleration theory. For AT 2020xnd, the most likely explanation for the significant flux excess at 10 GHz is the source geometry: a model of an inhomogeneous medium was successfully used to explain the shallow optically thick index observed in AT 2018cow (Nayana & Chandra 2021). We do not attempt to fit the spectrum of GRB 130925A: As an ultrarelativistic event, the framework presented here and in Margalit & Quataert (2021) is not directly applicable.

Our finding that the characteristic frequency of the thermal electrons ν_T is significantly below the observed peak frequency $\nu_T \ll \nu_{\text{peak}} = \nu_a$ and that the thermal electrons could dominate the observed emission all the way up to a factor of $\nu \sim 10^2 \times \nu_T$, may seem counterintuitive. We defer a detailed discussion of how this can be the case to Margalit & Quataert (2021). In summary, Margalit & Quataert (2021) show that if most of the electrons are in a thermal distribution, synchrotron emission from the thermal electrons can dominate most of the observed

emission. They define a frequency ν_j , the frequency at which the contribution from the thermal electrons equals the contribution from the power-law electrons: the thermal population dominates the emission at $\nu < \nu_j$ and the power-law population dominates the emission at $\nu > \nu_j$. They show that ν_j can be orders of magnitude larger than ν_T (in their notation, $\nu_\Theta = \nu_T$). Indeed, later in this section we directly constrain the ratio of power-law electrons to thermal electrons to be $\lesssim 0.16$.

We now use our inferred Maxwellian parameters to estimate the physical properties of the shock, summarized in Table 3. The characteristic synchrotron frequency of thermal electrons ν_T is determined by the electron temperature $\Theta = k_b T_e / m_e c^2$ and the magnetic field strength,

$$\nu_T = \Theta^2 \frac{eB}{2\pi m_e c}. \quad (13)$$

Assuming that the electron temperature is set by the postshock energy density (i.e., that electrons are in equilibrium with the ions), we can relate this quantity to the shock velocity,

$$\Theta \equiv \frac{k_b T_e}{m_e c^2} \approx \frac{3m_p v^2}{32m_e c^2} \approx 15.5 \left(\frac{v}{0.3c} \right)^2. \quad (14)$$

This implies that the thermal synchrotron frequency is

$$\nu_T \approx 0.67 \text{ GHz} \left(\frac{v}{0.3c} \right)^4 \left(\frac{B}{1 \text{ G}} \right) \quad (15)$$

and depends sensitively on the shock velocity. The flux density at this frequency within the SSA optically thick regime ($\tau_m \gg 1$; as is applicable in our current situation) is simply given by the Rayleigh–Jeans limit,

$$f_m = \frac{8\pi^2 m_e R^2 \nu_T^2 \Theta}{4\pi D^2} \approx 7.45 \times 10^{-10} \text{ mJy} \left(\frac{B}{1 \text{ G}} \right)^2 \left(\frac{v}{0.1c} \right)^{12} \left(\frac{t}{50 \text{ days}} \right)^2, \quad (16)$$

where D is the luminosity distance (1261 Mpc for AT 2020xnd) and $R \approx vt$ is the physical size (radius) of the emitting region. The latter approximation may be incorrect by a factor of a few if the geometry is aspherical or if the blast wave has been decelerating as a function of time.

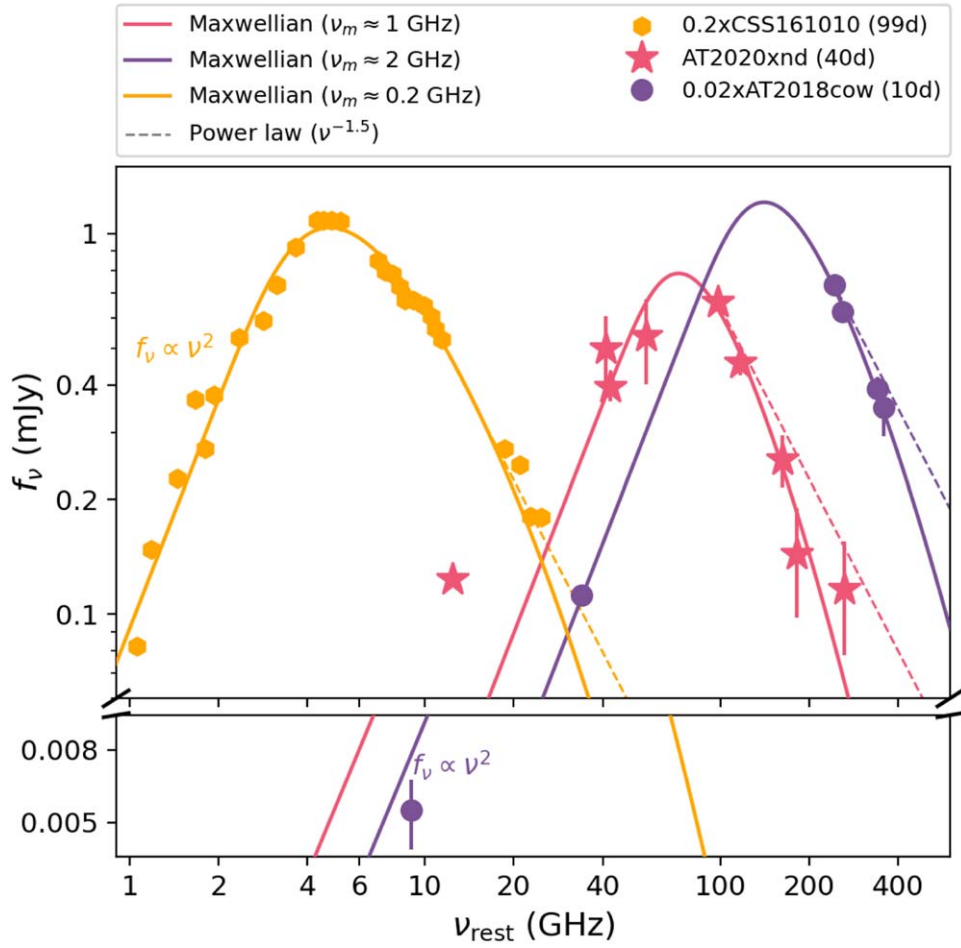


Figure 11. Radio and millimeter SEDs of cosmic explosions in the literature with inferred values of $p \geq 3.5$: AT 2018cow (circles; Ho et al. 2019b), CSS 161010 (hexagons; Coppejans et al. 2020), and AT 2020xnd (stars; this paper). Each SED is well described by a self-absorbed relativistic Maxwellian (i.e., $\nu_T < \nu_d$), shown as solid lines. For reference, we show a “limiting case” power law with $\beta = -1.5$ as a dotted line: such a steep power law is already difficult to explain in the context of diffuse shock-acceleration theory. For clarity, the light curves of AT 2018cow and CSS 161010 have been scaled in flux by factors of 0.02 and 0.2, respectively.

Table 3

Quantities Derived from Fitting an Absorbed Relativistic Maxwellian to the SEDs of AT 2020xnd, AT 2018cow, and CSS 161010 shown in Figure 11

Parameter	AT 2020xnd (40 days)	AT 2018cow (10 days)	CSS 161010 (99 days)
f_m (mJy)	0.0003	0.04	0.03
τ_m	6×10^4	2×10^4	7×10^2
ν_T (GHz)	0.7	2	0.2
v/c	0.3	0.3	0.5
B (G)	1	4	0.04
n_e (cm $^{-3}$)	4×10^3	9×10^3	40

Finally, we can estimate the ambient density from the optical depth parameter τ_m , which is given by

$$\tau_m = \frac{\pi e}{2\sqrt{3}} \frac{n_e R}{\Theta^5 B} \approx 3.73 \times 10^7 \left(\frac{n_e}{100 \text{ cm}^{-3}} \right) \left(\frac{B}{1 \text{ G}} \right)^{-1} \left(\frac{v}{0.1c} \right)^{-9} \left(\frac{t}{50 \text{ days}} \right). \quad (17)$$

For AT 2020xnd, AT 2018cow, and CSS 161010, we find values of v , B , and n_e that are physically realistic (Table 3) and quite similar to the values derived under the assumption of a pure power-law electron distribution. The fact that the inferred

parameters are similar under the thermal and power-law assumptions is not surprising; see Figure 2 of Margalit & Quataert (2021).

Finally, we consider whether the Maxwellian could also be used to describe the late-time data of AT 2020xnd (from Section 3.1). We fit each epoch independently and show the fits in Figure 12, again excluding the 6 GHz measurement. Fitting each epoch independently, we find $v \approx 0.3c$, $B = 0.2$ G, and $n_e = 840 \text{ cm}^{-3}$ in the first epoch, $v \approx 0.2c$, $B = 0.4$ G, and $n_e = 148 \text{ cm}^{-3}$ in the second epoch, and $v \approx 0.2c$, $B = 0.7$ G, and $n_e = 37 \text{ cm}^{-3}$ in the third epoch.

With this model, we can directly constrain the fraction of electrons that were accelerated into a power-law distribution based on the fact that we do not observe a transition from an exponential to a power law in the SED, the frequency defined as ν_j in Margalit & Quataert (2021). The frequency ν_j is directly related to the relative number of electrons in this power-law distribution to those in the thermal distribution. Taking the data at 46 days (rest-frame), we estimate that $\nu_j \gtrsim 200$ GHz. The ratio of this transition frequency to the “thermal” synchrotron frequency is $x_j \equiv 2\nu_j/3\nu_T \gtrsim 190$.

Assuming $\Theta \gtrsim 1$ and that the minimum Lorentz factor of electrons within the putative power-law distribution is $\gamma_m = 3\Theta$ (the mean Lorentz factor of thermal electrons), the ratio δ of

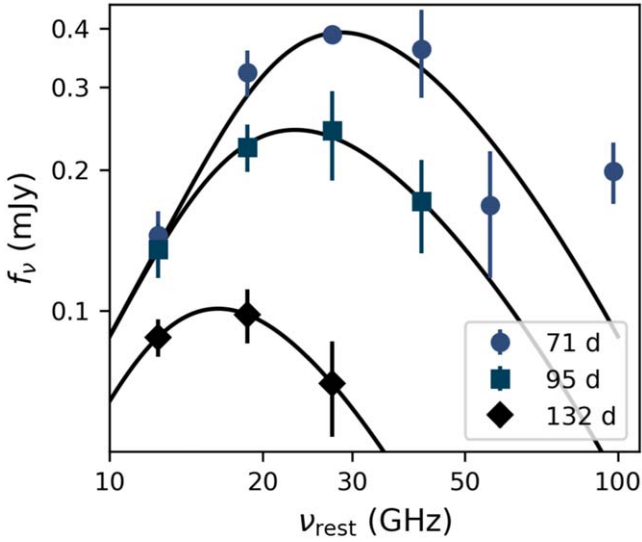


Figure 12. Maxwellian fits to late-time low-frequency VLA observations of AT 2020xnd. Each color/symbol combination corresponds to a different observer-frame epoch, the same as in Figure 3. The flux-density values have a basic cosmological correction applied and frequency values are reported in the rest frame.

energy in the power-law distribution versus the thermal distribution determines the transition frequency ν_j . Using the results of Margalit & Quataert (2021) we find that our observational constraint $x_j \gtrsim 190$ implies that $\delta \lesssim 0.16$ for any $2.2 \leq p \leq 3.2$ (with very weak p dependence). If the thermal electron population carries a fraction $\epsilon_T \sim 1$ of the total postshock energy, then $\delta = \epsilon_e/\epsilon_T$ can be interpreted as $\sim \epsilon_e$, the fraction of postshock energy that goes into accelerating nonthermal electrons. Our interpretation above would constitute a novel constraint on this parameter.

If the Maxwellian model is correct, the question is why we are seeing a thermal electron distribution in this group of objects (AT 2018cow, AT 2020xnd, and CSS 161010) and why this has not been inferred from radio observations of SNe. Ho et al. (2019b) showed that the luminous millimeter emission observed in AT 2018cow implied a high ambient density. It is tempting to think that the high ambient density could lead to electron collisions, which could in turn produce a thermal distribution. However, as shown in Figure 9, similarly high ambient densities have been observed in radio SNe (e.g., Soderberg et al. 2005; Dong et al. 2021) with no evidence for a sharp high-frequency cutoff or an $f_\nu \propto \nu^2$ optically thick spectrum. So, density cannot be the only important factor. We defer a detailed discussion of the physical conditions under which a relativistic Maxwellian component is observable to Margalit & Quataert (2021). In summary, the prominence of the thermal population is primarily determined by the shock speed, with a secondary dependence on the ambient density. In other words, the prominence of the Maxwellian in AT 2018cow, CSS 161010, and AT 2020xnd is due to the fact that these events have both faster shock speeds and higher ambient densities than most observed cosmic explosions.

3.2.3. Non-steady-state Particle Acceleration

So far, we have been assuming that the millimeter emission arises from continuous shock acceleration. Indeed, the framework typically used to model SNe assumes that particle injection is in a steady state. Beyond SN studies, however,

other classes of radio sources show very steep spectral indices—such as active galactic nuclei (AGNs) that are “switched off” (e.g., Cohen et al. 2005; Shulevski et al. 2015). When particle acceleration is not in a steady state, the optically thin spectral index can be arbitrarily steep, as the highest-energy electrons cool fastest.

In this section we explore the possibility that in AT 2020xnd shock acceleration was also not continuous. We consider a scenario in which shock acceleration switches off and the electrons cool through inverse Compton scattering, synchrotron emission, or adiabatic expansion. First we estimate the dynamical time at 46 days (observer frame), the epoch when the steep optically thin spectral index was measured, as a basis of comparison for the cooling processes:

$$t_{\text{dyn}} \sim \frac{R}{v} \sim (20 \text{ days}) \left(\frac{R}{10^{16} \text{ cm}} \right) \left(\frac{v}{0.2c} \right)^{-1}. \quad (18)$$

At 46 days, the shock speed $v \approx 0.2c$ and $R \approx 2 \times 10^{16}$ cm, so $t_{\text{dyn}} \approx 40$ days. Next we estimate the synchrotron-cooling time at 100 GHz. Taking the Lorentz factor of the electrons emitting at $\nu = 100$ GHz to be $\gamma = (2\pi m_e c \nu / (eB))^{1/2}$, we have

$$t_{\text{syn}} \approx \frac{6\pi m_e c}{\sigma_T B^2 \gamma} \approx (50 \text{ days}) \left(\frac{B}{1 \text{ G}} \right)^{-3/2}. \quad (19)$$

At 46 days, we have $B \approx 1$ G, so $t_{\text{syn}} \approx 50$ days, which is comparable to the dynamical time.

Finally, we estimate the cooling timescale from inverse Compton scattering by replacing B^2 in the expression above with $8\pi u_{\text{ph}}$, where u_{ph} is the photon energy density measured from UVOIR observations,

$$\begin{aligned} t_{\text{IC}} &\approx \frac{3m_e c}{4\sigma_T u_{\text{ph}} \gamma} \\ &\approx (70 \text{ days}) \left(\frac{R}{10^{16} \text{ cm}} \right)^2 \left(\frac{L_{\text{UVOIR}}}{10^{42} \text{ erg s}^{-1}} \right)^{-1} \left(\frac{B}{1 \text{ G}} \right)^{1/2}. \end{aligned} \quad (20)$$

We estimate that the optical luminosity at $\Delta t = 46$ days (observer frame) is $10^{42} \text{ erg s}^{-1}$ (Margutti et al. 2019; Perley et al. 2021). Again taking the forward-shock radius $R = 2 \times 10^{16}$ cm, we have $t_{\text{IC}} \approx 280$ days, longer than the dynamical time. As the cooling timescales from synchrotron radiation and inverse Compton scattering do not appear to be significantly shorter than the dynamical timescale, we conclude that it is unlikely that the “shutoff” of shock acceleration followed by rapid cooling can explain the steep spectrum observed at ~ 100 GHz.

Because the dynamical time of 40 days is similar to the synchrotron-cooling time of 50 days, we next consider whether the expansion of the emitting region (adiabatic cooling) could explain the radio light curves. In particular, because the picture of shock-interaction with a dense shell has been invoked to explain AT 2018cow (Margutti et al. 2019; Perley et al. 2019) as well as other fast and luminous optical transients (Ofek et al. 2010; Rest et al. 2018; Ho et al. 2019a; Leung et al. 2021), it is interesting to consider whether the same region that produced the optical emission could have expanded and also produced the radio emission. This is plausible, because the radius of the region responsible for the optical emission is roughly 10^{14} cm (Margutti et al. 2019; Perley et al. 2019), which would be roughly 10^{16} cm by 18 days in the observer frame assuming

$v = 0.2c$; furthermore, because the electron synchrotron-cooling timescale is long, there may still be relativistic electrons left to radiate when the shell expands to this radius.

For adiabatic expansion, we have $R \propto t$, $B \propto R^{-2} \propto t^{-2}$ (by flux conservation), and $N_0 \propto R^{-(2+p)} \propto t^{-(2+p)} \propto t^{-5}$ for $p = 3$, where the electron-energy distribution is $N(E) = N_0 E^{-p}$. At a given frequency in the optically thin $\nu > \nu_a$ regime, we therefore expect $f_\nu \propto R^3 N_0 B^{(p+1)/2} \propto t^{-6}$ (Chevalier 1998). At a given frequency in the optically thick regime, we expect $f_\nu \propto R^2 B^{-1/2} \nu^{5/2} \propto t^3$.

Finally, the evolution of ν_a and F_a can be estimated from Appendix C. We find that $F_a \propto t^{-3.5}$ and $\nu_a \propto t^{-2.6}$ under the same assumptions above. So, the adiabatic expansion of a shocked shell—without continuous shock acceleration—can result in steeply declining light curves and steeply declining values of F_a and ν_a . Our observations of AT 2020xnd do not quite match the predicted values, however; the observed temporal decline of F_a and ν_a are shallower than expected, and the light curves at optically thick and thin frequencies are slightly shallower. So, we also consider this picture unlikely.

3.3. Summary and Model Comparison

In this section, we considered three possible explanations for the early millimeter emission in AT 2020xnd. First we considered the standard framework used in the literature, synchrotron emission from electrons accelerated into a power-law energy distribution. The challenge for this model is that it implies that the measured spectral index of $\beta = -2.0 \pm 0.2$ implies an electron-energy power-law index of $p = 4.0 \pm 0.5$, significantly steeper than the predicted $p = 2$ from diffuse shock acceleration and—to our knowledge—steeper than all radio SNe in the literature. The very steep spectrum led us to consider an alternate model: synchrotron emission from electrons in a thermal distribution. As shown in Figure 11, the thermal model naturally explains the $f_\nu \propto \nu^2$ self-absorbed power-law index observed in CSS 161010, as well as the steep high-energy spectral index in AT 2018cow, AT 2020xnd, and CSS 161010. The primary challenge for this model is the fact that it has not been inferred for other cosmic explosions. However, as discussed in detail in Margalit & Quataert (2021), the prominence of thermal electron emission can naturally be explained by the unusual mildly relativistic shock speeds of these events. While it may at first seem surprising that the thermal population dominates the emission even at frequencies two orders of magnitude larger than the peak frequency at which the thermal electrons radiate, this is expected when the nonthermal population only has a modest fraction of the total energy of the shock-accelerated electrons, as has been shown in previous work in the context of AGNs (e.g., Özel et al. 2000). Finally, we considered two scenarios in which the emission arises from non-steady-state particle acceleration. However, we concluded that both scenarios were unlikely: The cooling time is not significantly shorter than the dynamical time, and adiabatic expansion predicts different values for the temporal evolution of the radio light curves.

All the possibilities listed above would be interesting. For example, if the electron distribution is a power law, then the inferred value of $p > 3.5$ is surprising given the wealth of observational and theoretical data favoring $p \sim 2$ –3. However, because of the shallow optically thick spectral index, the steep optically thin spectral index, and the natural explanation for the prominent thermal emission presented in Margalit & Quataert

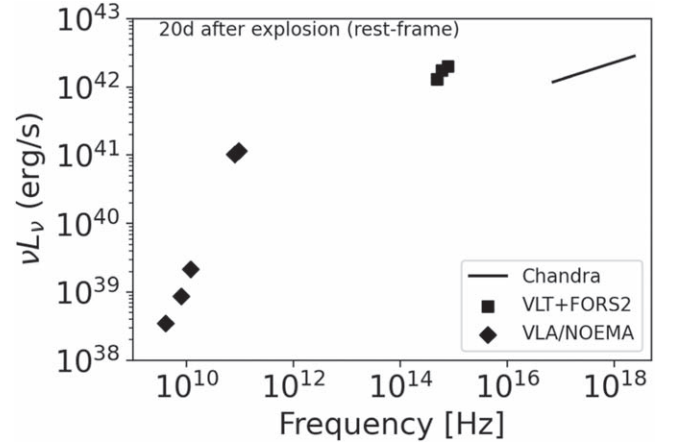


Figure 13. SED of AT 2020xnd at 26 days after explosion (observer frame) or 21 days in the rest frame. The optical data are taken from Perley et al. (2021). We plot the Chandra data as follows: We take the integrated 0.3–10 keV flux, use the geometric mean of (0.3, 10 keV), and the spectral index $f_\nu \propto \nu^{-0.75}$ to solve for the normalization coefficient for the spectrum. We display the spectrum over the full 0.3–10 keV range.

(2021), we conclude that the theoretically simplest explanation is the presence of a thermal population in addition to a nonthermal tail. In Section 6 we present observational tests that can rule out or confirm this model in the future.

4. Origin of the X-Ray Emission

In the previous section, we considered the origin of the radio and millimeter-band emission. In this section we consider the origin of the X-rays, which were one of the most peculiar features of AT 2018cow. The X-rays observed from AT 2018cow could not be described as an extension of the radio synchrotron spectrum, nor by inverse Compton scattering of UVOIR photons by electrons accelerated in the forward shock; the conclusion was that they must arise from a central compact source (Margutti et al. 2019; Ho et al. 2019b). We find that similar arguments hold for AT 2020xnd, although the X-ray data are more limited in temporal resolution and sensitivity.

In Figure 13 we plot the SED from radio to X-ray bands at $\Delta t \sim 26$ days (observer frame; MJD 59,158). The radio to X-ray spectral index at this time is $\beta_{RX} \approx 0.2$ where $f_\nu \propto \nu^{-\beta}$. Therefore, the value of β_{RX} is too shallow for the X-rays to be an extension of the synchrotron spectrum.

Next we consider the possibility that the X-rays arise from inverse Compton scattering. We begin with the energetics. The X-ray lightcurve of AT 2020xnd is similar to that of AT 2018cow in showing a plateau phase followed by a decline phase (Figure 5). Assuming that the plateau extends to 30 days, we estimate that the total X-ray energy emitted in the first month is 10^{49} erg, similar to the 7×10^{48} erg inferred from the AT 2018cow X-ray emission and similar to the energy we estimated from the AT 2020xnd radio observations. Therefore, if a significant proportion of the X-rays is produced by inverse Compton emission, then our assumption of $\epsilon_e = \epsilon_B = 1/3$ results in a significant underestimate of the total energy.

The ratio of the X-ray to radio luminosity at $\Delta t \approx 26$ days is $L_X/L_{\text{radio}} \approx 40$ –80, close to the value of 30 for AT 2018cow. If the X-rays arise from inverse Compton scattering off the

Table 4
The Rates of Transients Similar to AT 2018cow in Millimeter Surveys, Compared to Other Classes of Millimeter-bright Cosmic Explosions

Class	Survey	Band (GHz)	Sensitivity (6σ) (mJy)	Area (% sky)	Horizon (Mpc)	Rate (yr^{-1})
AT 2018cow	SPT-3G	95	15	4%	330	0.4
	ACT	100	90	40%	140	0.3
	CMB-S4 Wide	95	18	50%	300	4
	CMB-S4 ultradeep	95	5	3%	590	2
LGRB	CMB-S4 Wide	95	18	50%	2200	2
	CMB-S4 ultradeep	95	5	3%	4200	1
LLGRB	CMB-S4 Wide	95	18	50%	68	0.2
	CMB-S4 ultradeep	95	5	3%	130	0.07
CC SN	CMB-S4 Wide	95	18	50%	7	0.05
	CMB-S4 ultradeep	95	5	3%	13	0.02

Note. The horizon is set by requiring a 6σ detection. For SPT-3G and CMB-S4 the sensitivity assumes one-week stacks because these surveys have a cadence of one observation per day or higher.

synchrotron-emitting electrons, we have

$$\frac{L_X}{L_{\text{radio}}} = \frac{L_{\text{IC}}}{L_{\text{syn}}} = \frac{u_{\text{ph}}}{u_B}, \quad (21)$$

where u_{ph} is again the photon energy density (measured from UVOIR observations) and u_B is the magnetic energy density (measured from our radio observations; Rybicki & Lightman 1986). From the previous section we have $u_{\text{ph}} \approx 0.03 \text{ erg cm}^{-3}$. We require $B \approx 0.03\text{--}0.1 \text{ G}$, where $u_B = B^2/8\pi$. This is smaller than our estimate from modeling the SED using a nonthermal or thermal electron energy distribution. In addition, the X-ray luminosity does not decline rapidly in keeping with the optical lightcurve, and the spectral index is shallower than would be expected. So, as was the case in AT 2018cow, we conclude that the X-rays are unlikely to arise from IC scattering.

5. Rates in Millimeter Surveys

Until recently, there was only one untargeted transient survey specific to the millimeter band (Whitehorn et al. 2016). Within the past year, the Atacama Cosmology Telescope (ACT; Thornton et al. 2016) and the South Pole Telescope (SPT; Carlstrom et al. 2011) published blind discoveries of bright (millijansky) transients (Naess et al. 2021; Guns et al. 2021), including several of extragalactic origin (Guns et al. 2021). The 100 GHz lightcurve of AT 2020xnd (Figure 2) is the most luminous ever obtained for a nonrelativistic cosmic explosion, and in this section, we estimate the rate of such events in present and future millimeter transient surveys, summarized in Table 4.

For the volumetric rate we use the result from Ho et al. (2021) that events similar to AT 2018cow occupy a tight region in optical transient parameter space, with a volumetric rate of 0.001%–0.1% of the core-collapse (CC) SN rate (Coppejans et al. 2020; Ho et al. 2021) or $0.7\text{--}70 \text{ yr}^{-1} \text{ Gpc}^{-3}$. We take a characteristic 100 GHz luminosity of $2 \times 10^{30} \text{ erg s}^{-1} \text{ Hz}^{-1}$. We estimate the number of detections per year assuming a 6σ threshold (as in Whitehorn et al. 2016).

We use the following survey parameters. The SPT surveys an area of 1500 deg^2 with a 6σ sensitivity of 15 mJy at 95 and 150 GHz in one-week stacks (Whitehorn et al. 2016). The ACT surveys $18,000 \text{ deg}^2$ (40% of the sky) in raster scan mode, scanning back and forth at constant elevation and allowing

sources to pass through the field of view. The cadence has been roughly one week since 2016. The 1σ sensitivity in a single sweep is 30–50 mJy at 90 GHz, but for a source that is steady across the time it takes to traverse the focal plane (approximately 10 minutes), this is reduced to 10–20 mJy. Here we take an rms sensitivity of 15 mJy. CMB-S4 (Abazajian et al. 2019), a next-generation cosmic microwave background (CMB) experiment, will conduct two surveys relevant for the discovery of transients like AT 2018cow: an all-sky wide-area survey (50% of the sky) and an ultradeep survey in a smaller region (3%). The CMB-S4 6σ sensitivity for one-week stacks is 18 mJy in the wide survey and 5 mJy in the deep survey (Abazajian et al. 2019).

To estimate the rate of other classes of energetic explosions, in particular long-duration GRBs and low-luminosity GRBs, we take rates from Table 10 of Ho et al. (2020b). The GRB luminosity function at 100 GHz is uncertain. de Ugarte Postigo et al. (2012) found an average peak spectral luminosity of $10^{32.1 \pm 0.7} \text{ erg s}^{-1} \text{ Hz}^{-1}$ among detected bursts, although the overall detection rate was only 25%. For now we adopt a characteristic luminosity of $10^{32} \text{ erg s}^{-1} \text{ Hz}^{-1}$. Slightly off-axis GRBs are expected to have a similar luminosity to those observed directly on axis (Metzger et al. 2015), so the correction from including off-axis bursts may roughly compensate for the correction for bursts that are millimeter-faint. For LLGRBs, we adopt a characteristic 100 GHz luminosity of $10^{29} \text{ erg s}^{-1} \text{ Hz}^{-1}$ (from Figure 1). For SNe, we adopt a 100 GHz luminosity of $10^{27} \text{ erg s}^{-1} \text{ Hz}^{-1}$ (again based on Figure 1).

The number of events detected per year is simply

$$N_{\text{det}} = \frac{4\pi}{3} d_{\text{lim}}^3 \times \mathcal{R} \times A_{\text{survey}}, \quad (22)$$

where d_{lim} is the distance out to which the transient can be detected (second-to-last column in Table 4), \mathcal{R} is the volumetric rate, and A_{survey} is the fraction of the sky observed by the given survey. For the millimeter-band surveys we assume that the duration of the transient is significantly longer than the cadence and therefore that all transients in that area within the given volume will be detected.

Table 4 shows that for an optimistic estimate of the rate (0.1% of the CC SN rate), events similar to AT 2018cow should be detected routinely by CMB-S4, with a per-year rate

higher than what is currently achieved by optical surveys, and that they may be a dominant population of cataclysmic extragalactic millimeter-band transients. However, for a more pessimistic estimate of 0.01% of the CC SN rate, the number of detected sources would be more similar to that predicted for LLGRBs and the expected number would be an order of magnitude less than that of LGRBs. An interesting scientific question will be whether other classes of cosmic explosions, such as SNe, exhibit millimeter behavior similar to that of AT 2018cow but are not particularly remarkable at optical wavelengths and therefore are not currently followed up at high frequencies.

Our predicted rates for AT 2018cow-like events are slightly higher than those predicted using more detailed simulations (Eftekhari et al. 2021). This is primarily because we used the observed 100 GHz lightcurve of AT 2020xnd, while the simulations used the 230 GHz lightcurve of AT 2018cow and scaled it to 100 GHz assuming $F_\nu \propto \nu^{-0.7}$. Our back-of-the-envelope estimate for LGRBs is consistent with the more detailed prediction for the CMB-S4 wide survey but significantly lower than the prediction for the deep survey. The differences may be due to the fact that the simulations incorporate the evolution of the cosmic star formation rate. We also point out that the detection rate of extragalactic transients is predicted to be dominated by the reverse shock from LGRBs (Eftekhari et al. 2021), which we have not considered here.

6. Summary and Discussion

We presented millimeter, radio, and X-ray observations of AT 2020xnd, a transient with luminous ($M \approx -21$ mag) and short-duration ($t_{1/2} \approx 3$ days) optical emission. Our early discovery enabled only the second-ever detailed high-frequency ($\nu \gtrsim 100$ GHz) observations of such an object.

AT 2018cow and AT 2020xnd comprise a growing class of objects with millimeter and radio properties that are unusual among cosmic explosions: a steep optically thin spectral index and early high-frequency emission that is difficult to reconcile with the late-time low-frequency behavior. The discrepancy between the early-time and late-time radio emission in AT 2020xnd was also noted by Bright et al. (2022), who suggested that it may arise from a steepening density distribution.

The basic shock properties from a standard analysis, assuming that the peak of the SED is governed by SSA and that the electrons are in a power-law distribution, are fast speed ($v \approx 0.2c$) and high ambient density, similar to that inferred for AT 2018cow. Furthermore, the X-ray emission is in excess of what would be predicted from an extrapolation of the synchrotron spectrum. Bright et al. (2022) independently reached a similar conclusion from their 1–100 GHz data. We also found that the X-rays are in excess of that predicted from inverse Compton scattering.

However, based on our 100–200 GHz NOEMA data, we conclude that a thermal electron distribution (a relativistic Maxwellian) likely significantly contributes to the synchrotron emission at early times and likely also contributed to the emission observed in AT 2018cow and CSS 161010. The Maxwellian model predicts an optically thick spectral index of $f_\nu \propto \nu^2$, which was observed in CSS 161010 and AT 2018cow; the optically thick spectral index of AT 2020xnd was even shallower.

The presence of a Maxwellian is not a surprise: It is expected that only a small fraction of electrons should be accelerated into

the power-law tail, with the majority accelerated into a thermal distribution (e.g., Park et al. 2015). The question then arises why it has not been definitively seen in previous SNe. As presented in more detail in Margalit & Quataert (2021), the detectability of the thermal population—its prominence relative to the nonthermal population, and its peak frequency—is highly sensitive to the shock speed (and to a lesser extent to the ambient density). The mildly relativistic shock speeds of transients like AT 2018cow, CSS 161010, and AT 2020xnd—together with the fact that early high-frequency observations were obtained—explains why the thermal population is more prominent in these events than in most observed SNe. The fast speed (and high ambient density) is also why the influence of the Maxwellian is best observed at high frequencies ($\gtrsim 100$ GHz). Testable predictions of this model are that the transition from the thermal to power-law distribution should be detectable in even higher-frequency observations ($\gtrsim 200$ GHz) and that explosions with fast shock speeds ($v \gg 0.1c$) should have ν^2 rather than $\nu^{5/2}$ optically thick spectral indices.

Accounting for the Maxwellian does not dramatically change the inferred physical parameters: The shock speeds remain in the range of 0.1–0.5 c , and the ambient densities are close to 10^4 cm^{-3} . However, for AT 2018cow, the Maxwellian model implies a shock speed of $\approx 0.3c$ at 10 days and a decelerating shock, different from the constant shock speed of 0.1 c inferred in previous work. In addition, it enables a novel constraint on the fraction of electrons accelerated by the shock, which we constrain to be $< 20\%$ from our observations of AT 2020xnd. We defer a thorough reanalysis of the evolution of AT 2018cow, CSS 161010, and AT 2020xnd in the context of a Maxwellian to future work. For now we caution that the usual assumption of all electrons being accelerated into a power-law distribution is not well motivated for fast shock speeds ($v \gtrsim 0.2c$) and high ambient densities for the observing frequencies involved here (1–100 GHz).

It appears that a short lightcurve duration and high peak luminosity are predictive of luminous millimeter and X-ray emission. Indeed, this sets AT 2018cow and AT 2020xnd apart from optical transients that have similar spectroscopic properties and rapid lightcurve evolution: interacting SNe of Type Ibn. This suggests that the essential difference between AT 2018cow and Type Ibn SNe is the presence of high-velocity ejecta, perhaps from a central engine like a newly formed black hole (Kashiyama et al. 2018; Quataert et al. 2019)—analogous to the fact that most stripped-envelope SNe do not exhibit relativistic ejecta, while a small subset (those associated with GRBs) do.

The limitation of our approach—identifying transients via optical surveys and following them up with millimeter telescopes—is that it prevents us from identifying the subset of other SN classes that may exhibit similar behavior. Indeed, a handful of transients had similar shock properties to AT 2018cow and AT 2020xnd, including SN 2003L and PTF 11qej. The shock properties, together with the observation of optically thick emission at early times, suggests that they would also have been luminous millimeter transients, perhaps also with a prominent Maxwellian component to the SED. Future wide-field millimeter cosmology experiments will enable luminous millimeter transients to be detected routinely without relying on an optical discovery. Based on our NOEMA 100 GHz lightcurve of AT 2020xnd, we estimate that events like AT 2018cow and AT 2020xnd (and likely other types of

SNe) will be detected blindly by CMB-S4. Our work is a direct demonstration of how these discoveries, together with multi-band follow-up observations, can shed light on the mechanism of particle acceleration in astrophysical shocks produced by cosmic explosions. The code used to produce the figures in this paper can be found in a public Github repository¹⁹.

A.Y.Q.H. would like to thank Eliot Quataert, Dan Kasen, Sterl Phinney, Anatoly Spitkovsky, and Shri Kulkarni for useful discussions about steep-spectrum radio sources and relativistic Maxwellians; Kunal Mooley for assistance with VLA calibration; Fabian Walter for advice regarding NOEMA data reduction; and Joe Bright, Greg Sivakoff, and Susan Clark for a careful reading of the manuscript. D. K. and A.O. are supported by NSF grant AST-1816492. B. M. is supported by NASA through the NASA Hubble Fellowship grant #HST-HF2-51412.001-A awarded by the Space Telescope Science Institute, which is operated by the Association of Universities for Research in Astronomy, Inc., for NASA, under contract NAS5-26555. The authors would like to thank the anonymous referee for detailed comments that greatly improved the clarity of the paper.

The Submillimeter Array is a joint project between the Smithsonian Astrophysical Observatory and the Academia Sinica Institute of Astronomy and Astrophysics and is funded by the Smithsonian Institution and the Academia Sinica.

This work is based on observations carried out under project numbers D20AF and D20AG with the IRAM NOEMA Interferometer. IRAM is supported by INSU/CNRS (France), MPG (Germany), and IGN (Spain).

The National Radio Astronomy Observatory is a facility of the National Science Foundation operated under cooperative agreement by Associated Universities, Inc.

The Australia Telescope Compact Array is part of the Australia Telescope National Facility (grid.421683.a), which is funded by the Australian Government for operation as a National Facility managed by CSIRO. We acknowledge the Gomeroi people as the traditional owners of the Observatory site.

The scientific results reported in this article are based in part on observations made by the Chandra X-ray Observatory. This research has made use of software provided by the Chandra X-ray Center (CXC) in the application package CIAO.

Facilities: EVLA, VLA, IRAM:NOEMA, SMA.

Software: CASA (McMullin et al. 2007), astropy (Astropy Collaboration et al. 2013, 2018), matplotlib (Hunter 2007), scipy (Virtanen et al. 2020), pyne2001.

Appendix A

Radio Observations and Reduction

A.1. Very Large Array (VLA)

Our VLA observations are summarized in Table 5. Observations were obtained in standard continuum imaging mode and spanned the BnA, A, and D configurations. We used 3C 48 as the flux density and bandpass calibrator and J2218–0335 as the complex gain calibrator. Data were calibrated using the automated pipeline available in the Common Astronomy Software Applications (CASA; McMullin et al. 2007), with additional flagging performed manually,

and imaged²⁰ using the CLEAN algorithm (Högbom 1974). In each image, we verified that the source was a point source using `imfit` and that the image was free of artifacts, then measured the peak flux density in a region centered on the source using `imstat`.

To estimate the uncertainty on the source flux density, we measured the rms pixel value in an area of the image close to the source with no substantial emission. We added this in quadrature to two additional sources of systematic error. First, the VLA flux-density scale calibration accuracy is 5% at the *L*-through *Ku* bands and 10%–15% for the three higher bands.²¹ Second, the flux-density calibrator 3C 48 has been undergoing a flare since 2018 January. To account for this, we added an additional 10% systematic error at low frequencies (*C* band through *Ku* band), an additional 15% at the *K* and *Ka* bands, and 20% at the *Q* band.

A.2. Australia Telescope Compact Array

We obtained three observations with the Australia Telescope Compact Array (ATCA) under project CX472, with two 2048 MHz bands centered on 33 and 35 GHz. Observations were carried out in the 6B, H168, and 1.5A array configurations, with maximum baselines of 6 km, 192 m (after removing antenna 6 to ensure more even sampling of the *u*–*v* plane), and 4.5 km.

The data were reduced using standard MIRIAD routines (Sault et al. 1995). The first and third observations used the standard continuum correlator setup with 1 MHz channels, while the second observation was carried out in a hybrid correlator mode with 1 MHz channels in the 33 GHz band and 64 MHz coarse channels in the 35 GHz band. A single zoom band with 2048×64 kHz channels was placed at 35 GHz to allow for the initial calibration of the coarse channels delays, although these data were not used further.

For all observations we performed an initial bandpass calibration using observations of 1921–293 and calibrated the gain and polarization using the secondary calibrator, 2216–038. We used 1934–638 to calibrate the flux-density scale and then improved the bandpass calibration using the standard bootstrapping procedure outlined in the ATCA User Guide.²² Both bands were combined and imaged with a cell size corresponding to approximately one-fifth of the synthesized beamwidth using CLEAN (Högbom 1974) and `robust=0.5` weighting. We used `IMFIT` to fit a point source, allowing the position to vary in a 20×20 pixel box centered on the location of AT 2020xnd and in the event of a detection, report the measured flux density and associated uncertainty. In the event of a nondetection we report an upper limit of 3 times the image noise.

We have also independently analyzed the ATCA observations reported by Bright et al. (2020a, 2020b) under project CX471, as well as a third epoch that was not reported. These observations were carried out with two 2048 MHz bands centered on 17 and 19 GHz with the same flux, bandpass, and phase calibrators described above. The same overall process

²⁰ The cell size was one-fifth that of the synthesized beamwidth, the field size was the smallest magic number (10×2^6) larger than the number of cells needed to cover the primary beam.

²¹ <https://science.nrao.edu/facilities/vla/docs/manuals/oss/performance/fdscale>

²² https://www.narrabri.atnf.csiro.au/observing/users_guide/html/atug.html#Calibration2

¹⁹ <https://github.com/annayqho/ZTF20acigmel>

Table 5
Observations of AT 2020xnd with the SMA, NOEMA, the ATCA, and the VLA

Start Date (UT)	Δt (days)	Facility	ν (GHz)	Flux Density (mJy)	Array Configuration
2020 Oct 20.1	10.1	SMA	230	<1.14	subcompact
2020 Oct 23.0	13.0	VLA	10	0.024 ± 0.006	BnA
2020 Oct 27.0	17.0	VLA	10	<0.024	BnA
2020 Oct 27.8	17.8	NOEMA	79	0.389 ± 0.059	10C
2020 Oct 27.8	17.8	NOEMA	94	0.304 ± 0.057	10C
2020 Oct 28.0	18.0	VLA	10	<0.051	BnA
2020 Oct 28.0	18.0	VLA	6	<0.030	BnA
2020 Oct 28.0	18.0	VLA	15	0.037 ± 0.010	BnA
2020 Oct 29.2	19.2	ATCA	34	<0.108	H168
2020 Oct 29.2	19.2 ^a	ATCA	18	0.135 ± 0.040	H168
2020 Oct 31.1	21.1	SMA	230	<0.48	subcompact
2020 Nov 02.8	23.8	NOEMA	79	0.675 ± 0.047	10C
2020 Nov 02.8	23.8	NOEMA	94	0.634 ± 0.045	10C
2020 Nov 04.0	25.0	VLA	15	0.095 ± 0.011	BnA
2020 Nov 04.0	25.0	VLA	10	0.057 ± 0.005	BnA
2020 Nov 04.0	25.0	VLA	6	0.046 ± 0.006	BnA
2020 Nov 07.3	28.3	ATCA	34	0.310 ± 0.020	H168
2020 Nov 10.8	31.8	NOEMA	79	1.076 ± 0.049	10C
2020 Nov 10.8	31.8	NOEMA	94	1.018 ± 0.044	10C
2020 Nov 14.1	35.1	SMA	230	<0.48	subcompact
2020 Nov 15.9	36.9	VLA	33	0.497 ± 0.011	BnA to A
2020 Nov 15.9	36.9	VLA	45	0.675 ± 0.171	BnA to A
2020 Nov 15.9	36.9	VLA	10	0.079 ± 0.010	BnA to A
2020 Nov 18.8	39.8	NOEMA	79	0.912 ± 0.050	10C
2020 Nov 18.8	39.8	NOEMA	94	0.825 ± 0.046	10C
2020 Nov 19.2	40.2 ^b	ATCA	18	0.320 ± 0.060	H168
2020 Nov 24.7	45.7	NOEMA	79	0.822 ± 0.048	10D
2020 Nov 24.7	45.7	NOEMA	94	0.569 ± 0.042	10D
2020 Nov 24.8	45.8	NOEMA	211	0.145 ± 0.048	10D
2020 Nov 24.8	45.8	NOEMA	227	<0.156	10D
2020 Nov 25.8	46.8	NOEMA	131	0.317 ± 0.049	9D
2020 Nov 25.8	46.8	NOEMA	146	0.179 ± 0.057	9D
2020 Nov 27.2	48.2	ATCA	34	0.490 ± 0.040	H168
2020 Nov 30.9	51.9	VLA	10	0.154 ± 0.005	BnA to A
2020 Nov 30.9	51.9	VLA	33	0.621 ± 0.132	BnA to A
2020 Nov 30.9	51.9	VLA	45	0.668 ± 0.168	BnA to A
2020 Dec 16.6 ^c	67.6	NOEMA	79	0.247 ± 0.037	11D
2020 Dec 16.6 ^c	67.6	NOEMA	94	<0.105	11D
2020 Dec 16.7 ^c	67.7	NOEMA	131	<0.213	9D
2020 Dec 16.7 ^c	67.7	NOEMA	146	<0.279	9D
2020 Dec 20.9	71.9	VLA	10	0.180 ± 0.023	A
2020 Dec 20.9	71.9	VLA	15	0.401 ± 0.046	A
2020 Dec 20.9	71.9	VLA	22	0.484 ± 0.010	A
2020 Dec 20.9	71.9	VLA	33	0.450 ± 0.096	A
2020 Dec 20.9	71.9	VLA	45	0.209 ± 0.063	A
2020 Dec 26.3	77.3	ATCA	18	0.300 ± 0.035	H168
2021 Jan 06.6	88.6	NOEMA	131	<0.114	11D
2021 Jan 06.6	88.6	NOEMA	146	<0.120	11D
2021 Jan 12.7	94.7	VLA	10	0.168 ± 0.022	A
2021 Jan 12.7	94.7	VLA	15	0.278 ± 0.032	A
2021 Jan 12.7	94.7	VLA	22	0.301 ± 0.065	A
2021 Jan 12.7	94.7	VLA	33	0.213 ± 0.048	A
2021 Feb 18.6	131.6	VLA	6	0.117 ± 0.016	A
2021 Feb 18.6	131.6	VLA	10	0.109 ± 0.010	A
2021 Feb 18.6	131.6	VLA	15	0.122 ± 0.016	A
2021 Feb 18.6	131.6	VLA	22	0.087 ± 0.020	A
2021 Feb 18.6	131.6	VLA	33	<0.042	A

Notes. Upper limits are reported as $3 \times$ the image rms (in the case of NOEMA, the rms of the UV plane fits). For NOEMA, the absolute flux-scale calibration accuracy is 5% at 3 mm, 15% at 2 mm and 20% at 1.3 mm. The VLA uncertainty is the quadrature sum of the image rms, the standard flux-density scale calibration accuracy (5% at the L through Ku bands, 15% for the K , Ka , and Q bands), and additional uncertainty from the fact that the flux-density calibrator 3C 48 is currently undergoing a flare (additional 10% at the C band through Ku band, 15% at the K and Ka bands, 20% at the Q band). All measurements are reported in the observer frame.

^a Reanalysis of the data first reported in ATel#14148.

^b Reanalysis of the data first reported ATel#14249.

^c Weather conditions unstable.

was used to reduce the data but substantially more manual flagging was carried out to remove data irregularities discovered via inspection of the visibilities. In all three observations we found noise spikes near the center of the 19 GHz band on some baselines²³ and flagged channels 500–1250 to remove them. In the third observation, we removed similar spikes at the edges of the 19 GHz band on baseline 1–2 (flagging channels 1–300 and 1800–2048) and near the center of the 19 GHz band on baselines 1–3 and 2–3 (flagging channels 850–1150). In the third observation, we also removed antenna 6 due to an irregular bandpass response and flagged all 19 GHz data from antenna 4 due to noise spikes in the Stokes YY visibilities across the full band.

A.3. The Submillimeter Array

We obtained three observations, all in the Sub-Compact configuration, using all eight antennas. During the first two observations, the receivers were tuned to local oscillator (LO) frequencies of 225.5 GHz USB and 232.5 GHz, which provide continuous frequency coverage from 209.5 to 249.5 GHz (with 10 GHz overlap) and 48 GHz bandwidth available for continuum channel generation. The third attempt piggybacked another science project with one of the receivers tuned to an LO of 225.3 GHz, giving coverage of 209.5 to 241.5 GHz while the second was tuned to an LO of 256.5 GHz giving coverage from 240.5 to 272 GHz (both with an 8 GHz gap in the middle between sidebands) giving a total of 48 GHz of bandwidth for continuum centered on 241.0 GHz. The quasars 2232+117 and 2148+069 were used as primary phase and amplitude gain calibrators, with absolute flux calibration performed by comparison to Neptune and Uranus, while the quasar 3C 84 was used for bandpass calibration. Data were calibrated in IDL using the MIR package then exported for additional analysis and imaging using the MIRIAD package. On the first night the atmospheric opacity was 0.22 (~ 4 mm precipital water vapor) and after 5.0 hr on source an rms of 0.38 mJy was achieved. The second night the opacity was 0.1, and after 5.0 hr on source an rms of 0.16 mJy was reached. On the final night the opacity was better (around 0.06) but with a shorter observation (4.3 hr on source) an rms of 0.16 mJy was again reached.

A.4. Northern Extended Millimeter Array

NOEMA is situated on the Plateau de Bure (France) at an altitude of 2550 m. The number of available 15 m antennas varied between 9 and 11, and the antenna spacings changed between intermediate-extended C and compact D configurations. The PolyFiX backend was configured in low-resolution continuum mode (2 MHz resolution) covering both sidebands of the 2SB receivers in dual polarization, resulting in a spectral coverage of 4×7.744 GHz. The spectral bandpass was calibrated on strong quasars and the time-dependent amplitude and phase calibrations done on the quasars 2216–038 and 2227–088 that are close to AT 2020xnd. In the primary flux calibration, the radio continuum of the emission-line stars MWC 349 and LKHA 101 was used; based on the observatory-internal flux monitoring

we assume that MWC 349 was 8% brighter at the time of the AT 2020xnd monitoring than its CLIC internal flux model predicts. This improves the overall consistency of the flux calibration in the 3 mm band from about 10% to 5%. The inherent errors of the 2 mm and 1.3 mm bands are higher, we assume them to be at 15% and 20%, respectively. The data reduction was done with the CLIC software (GILDAS package²⁴). Dual-polarization UV tables were written for each of the receiver sidebands; their central sky frequencies are given in Table 5. The resulting calibrated UV tables were analyzed in the MAPPING software (also from the GILDAS package) and point-source UV plane fits were performed. We constrained the fit position to the coordinates found in our VLA observations (Section A.1), the difference in the derived flux as compared to a free fit is typically a small fraction of one sigma. The advantage of this procedure compared to map deconvolution is the straightforward error propagation in the UV-fitting process. Weather conditions were good, with the exception of the 3 and 2 mm data points taken on 2020 December 16.

Appendix B X-Ray Observations and Reduction

We used the CIAO v4.12 (Fruscione et al. 2006) tool `specextract` to extract the spectrum, using a circular region with a radius of $1''$ centered on the apparent position of the source. The background was extracted from a nearby source-free region with a radius of $10''$. We performed spectral fitting on the 0.5–8 keV spectrum with `xspec` v12.11.0 (Arnaud 1996), using C-statistics via `cstat` (Cash 1979). We adopted an absorbed power-law model (`tbabs*power-law` in `xspec`, Wilms et al. 2000) and fixed the column density at the Galactic value of $N_H = 6.33 \times 10^{20} \text{ cm}^{-2}$ (Willingale et al. 2013). The resulting power-law photon index Γ and the 0.3–10 keV flux are listed in Table 6.

In the 3rd–6th observations, AT 2020xnd was not clearly detected. In order to determine the position of the source, we first ran `wavdetect` on the observations to obtain lists of positions for all sources in the Chandra ACIS-S3 FoV. We then cross-matched the Chandra source lists with the Gaia DR2 catalog (Gaia Collaboration et al. 2018) to obtain the astrometric shifts. For obsID 23549, $\delta R.A. = -0''.73 \pm 0''.12$ and $\delta \text{decl.} = -0''.93 \pm 0''.49$. For obsID 23550, $\delta R.A. = -0''.75 \pm 0''.14$ and $\delta \text{decl.} = -0''.45 \pm 0''.69$. For obsID 23551, $\delta R.A. = 0''.03 \pm 0''.23$ and $\delta \text{decl.} = 0''.66 \pm 0''.44$. For obsID 25008, $\delta R.A. = -0''.26 \pm 0''.33$ and $\delta \text{decl.} = 1''.02 \pm 0''.19$.

We used `srcflux` to estimate the 0.5–7 keV count rate and the uncertainty. For obsID 23549, two counts were detected in a $1''.5$ circular region, corresponding to a 2.46σ (Gaussian equivalent) confidence-limit detection. For obsID 23550, no count was detected in a $1''.7$ circular region. For obsID 23551, one count was detected in a $1''.5$ circular region, corresponding to a 1.75σ (Gaussian equivalent) confidence-limit detection. For obsID 25008, no count was detected in a $1''.4$ circular region. We then converted the count rate to 0.3–10 keV flux with `WebPIMMS`²⁵, assuming an absorbed power-law model with $\Gamma = 1.5$ and $N_H = 6.33 \times 10^{20} \text{ cm}^{-2}$.

²³ Baselines 3–4, 3–5 and 4–5 in the first observation; 1–4, 2–3, 3–4, 3–5 in the second; and 1–2 in the third.

²⁴ <https://www.iram.fr/IRAMFR/GILDAS/>

²⁵ <https://heasarc.gsfc.nasa.gov/cgi-bin/Tools/w3pimms/w3pimms.pl>

Table 6
Chandra Observations of AT 2020xnd

ObsID	Exp. Time (ks)	Obs. Time (MJD)	Δt (days)	0.5–7 keV Count Rate (10^{-3} count s^{-1})	Γ	0.3–10 keV Flux (10^{-14} erg cm^{-2} s^{-1})
23547	19.82	59,157.8	20.8	$1.24^{+0.28}_{-0.25}$	1.23 ± 0.48	$3.46^{+0.96}_{-1.27}$
23548	19.82	59,163.8	25.6	$1.24^{+0.28}_{-0.25}$	$1.75^{+0.56}_{-0.54}$	$2.79^{+0.75}_{-0.67}$
23549	19.82	59,179.1	37.9	$0.09^{+0.10}_{-0.06}$	1.5 (fixed)	$0.15^{+0.17}_{-0.11}$
23550	19.75	59,207.2	60.5	<0.13	1.5 (fixed)	<0.24
23551	16.86	59,316.6	148.5	<0.23	1.5 (fixed)	<0.44
25008	19.82	59,317.1	148.9	<0.13	1.5 (fixed)	<0.24

Notes. For obsID 23547–23549, all uncertainties are represented by the 68% confidence intervals. For the last three obsIDs, the limits are given by the upper bound of the 90% confidence intervals. Δt is rest-frame days since the reference epoch of 591,32 MJD.

Appendix C Synchrotron Self-absorption Model

Below, we derive expressions for the source properties (size, magnetic field, density) as a function of observationally accessible properties, specifically the self-absorption frequency ν_a and the corresponding (peak) flux $F_a \equiv f_\nu(\nu_a)$. Following the notation in the main text, we assume a spherical shock of radius R that propagates into an upstream medium whose density profile is $\rho \propto r^{-k}$. Similar to the standard Chevalier (1998) model, we assume that a nonthermal population of electrons is accelerated at the shock front and that magnetic fields are amplified behind it; that the energy density of relativistic electrons is a factor ϵ of the magnetic field energy density²⁶; that the nonthermal electron population can be modeled as a power law in Lorentz factor, $dN/d\gamma \propto \gamma^{-p}$, above $\gamma > \gamma_m$; and that the minimum Lorentz factor is $\gamma_m \approx 1$ and does not evolve with time. The final assumption follows the standard Chevalier (1998) hypothesis. We note however that an alternative hypothesis—related to the so-called deep-Newtonian regime first discussed by Sironi & Giannios (2013)—assumes that ϵ_e accounts for the energy of all electrons participating in diffusive-shock acceleration (not only those that are relativistic) and is akin to an effectively time-dependent γ_m (Sironi & Giannios 2013). In the present work, we focus on the “standard” model (Chevalier 1998) and leave consideration of the “deep-Newtonian” ansatz for future work.

The self-absorption frequency ν_a is defined as the frequency at which asymptotic expressions for the optically thin and optically thick flux equal one another, $f_\nu^{\text{thin}}(\nu_a) = f_\nu^{\text{thick}}(\nu_a)$. In the standard, slow-cooling, case where $\nu_a < \nu_c$ (here ν_c is the cooling frequency), this leads to the relations

$$R = \eta_1^{-\frac{p+4}{2(2p+7)}} \zeta^{-\frac{p+6}{2p+13}} \epsilon^{-\frac{1}{2p+13}} (F_a D^2)^{\frac{p+6}{2p+13}} \nu_a^{-1}, \quad (C1)$$

$$B = \eta_1^{-\frac{2(p+4)}{2p+13}} \zeta^{\frac{2}{2p+13}} \epsilon^{-\frac{4}{2p+13}} (F_a D^2)^{-\frac{2}{2p+13}} \nu_a, \quad (C2)$$

between the source size and magnetic field (R , B) and self-absorption frequency ν_a , flux density F_a , and angular-diameter distance D (see Bright et al. 2022 for a discussion of the various required cosmological corrections). Note that the measured peak flux is expected to be slightly smaller than F_a (as defined above) because the transition between the optically thin/thick limits, in reality, is smooth (and depends on geometry) rather than a broken power law.

²⁶ This is related to ϵ_e (ϵ_B), which is often used to express the ratio of electron (magnetic field) energy density to the total kinetic shock power via $\epsilon \equiv \epsilon_e/\epsilon_B$.

Above, we have defined the constants

$$\eta_1(p) \equiv \left[\frac{(p-2)\sigma_T}{12\pi^2 m_e^2 c} \right]^{\frac{2}{p+4}} \left(\frac{e}{2\pi m_e c} \right)^{\frac{p-2}{p+4}} \approx [(p-2) \times 2.26 \times 10^{17}]^{\frac{2}{p+4}} (2.80 \times 10^6)^{\frac{p-2}{p+4}} \quad (C3)$$

and

$$\zeta \equiv \frac{1}{3} (2\pi m_e)^{3/2} (c/e)^{1/2} \approx 1.14 \times 10^{-30}, \quad (C4)$$

where the numerical values are given in cgs units.

For the specific case where $p = 3$, we find

$$R \approx (5.1 \times 10^{15} \text{ cm}) \epsilon^{-1/19} \left(\frac{F_a}{\text{Jy}} \right)^{9/19} \times \left(\frac{D}{\text{Mpc}} \right)^{18/19} \left(\frac{\nu_a}{5 \text{ GHz}} \right)^{-1}, \quad (C5)$$

$$B \approx (0.30 \text{ G}) \epsilon^{-4/19} \left(\frac{F_a}{\text{Jy}} \right)^{-2/19} \left(\frac{D}{\text{Mpc}} \right)^{-4/19} \left(\frac{\nu_a}{5 \text{ GHz}} \right). \quad (C6)$$

This is consistent with the results of Chevalier (1998).

We now also consider the novel regime where the cooling frequency is below the self-absorption frequency. In this limit, we instead find

$$R = \xi^{\frac{1}{2(2p+7)}} \eta_1(p)^{-\frac{p+4}{2(2p+7)}} \zeta^{-\frac{p+3}{2p+7}} \times \epsilon^{-\frac{1}{2p+7}} (F_a D^2)^{\frac{p+3}{2p+7}} \nu_a^{-\frac{2p+5}{2p+7}} t^{\frac{1}{2p+7}}, \quad (C7)$$

$$B = \xi^{\frac{2}{2p+7}} \eta_1(p)^{-\frac{2(p+4)}{2p+7}} \zeta^{\frac{2}{2p+7}} \times \epsilon^{-\frac{4}{2p+7}} (F_a D^2)^{-\frac{2}{2p+7}} \nu_a^{\frac{2p+15}{2p+7}} t^{\frac{4}{2p+7}}, \quad (C8)$$

where the solution now depends explicitly on the elapsed time t , and the constant ξ in cgs units is given by

$$\xi \equiv \frac{\sigma_T^2}{18\pi m_e c e} \approx 5.97 \times 10^{-25}. \quad (C9)$$

Focusing again on the case where $p = 3$, we find that in the fast-cooling regime ($\nu_c < \nu_a$)

$$R \approx (4.2 \times 10^{15} \text{ cm}) \epsilon^{-1/13} \left(\frac{F_a}{\text{Jy}} \right)^{6/13} \times \left(\frac{D}{\text{Mpc}} \right)^{12/13} \left(\frac{\nu_a}{5 \text{ GHz}} \right)^{-11/13} \left(\frac{t}{100 \text{ day}} \right)^{1/13}, \quad (C10)$$

$$B \approx (0.14 \text{ G}) \epsilon^{-4/13} \left(\frac{F_a}{\text{Jy}} \right)^{-2/13} \left(\frac{D}{\text{Mpc}} \right)^{-4/13} \times \left(\frac{\nu_a}{5 \text{ GHz}} \right)^{21/13} \left(\frac{t}{100 \text{ days}} \right)^{4/13}. \quad (\text{C11})$$

The number density of relativistic electrons $n_{e,\text{rel}}$ (those with Lorentz factor $> \gamma_m$) can then be inferred using the magnetic field expressions above; it is

$$n_{e,\text{rel}} = \frac{p-2}{p-1} \epsilon \frac{B^2}{m_e c^2} \approx \begin{cases} (5.5 \times 10^4 \text{ cm}^{-3}) \epsilon^{11/19} \left(\frac{F_a}{\text{Jy}} \right)^{-4/19} \left(\frac{D}{\text{Mpc}} \right)^{-8/19} \left(\frac{\nu_a}{5 \text{ GHz}} \right)^2, & \nu_a < \nu_c \\ (1.2 \times 10^4 \text{ cm}^{-3}) \epsilon^{5/13} \left(\frac{F_a}{\text{Jy}} \right)^{-4/13} \left(\frac{D}{\text{Mpc}} \right)^{-8/13} \left(\frac{\nu_a}{5 \text{ GHz}} \right)^{42/13} \left(\frac{t}{100 \text{ day}} \right)^{8/13}, & \nu_a > \nu_c \end{cases}. \quad (\text{C12})$$

This is related to the upstream density n as $n \approx n_{e,\text{rel}} \times 2\gamma_m \epsilon_e^{-1} (m_e/m_p) (v/c)^{-2} (p-1)/(p-2)$, where v is the shock velocity.

One can verify the regime of relevance, i.e., whether $\nu_a \lesssim \nu_c$, by comparing ν_a from the expressions above, to $\nu_c = 18\pi m_e c e / \sigma_T^2 B^3 t^2$. This gives

$$\frac{\nu_a}{\nu_c} \approx \begin{cases} 6.2 \times 10^{-3} \epsilon^{12/19} \left(\frac{F_a}{\text{Jy}} \right)^{6/19} \left(\frac{D}{\text{Mpc}} \right)^{12/19} \left(\frac{\nu_a}{5 \text{ GHz}} \right)^{-3} \left(\frac{t}{100 \text{ day}} \right)^{-2}, & \nu_a < \nu_c \\ 5.9 \times 10^{-4} \epsilon^{12/13} \left(\frac{F_a}{\text{Jy}} \right)^{6/13} \left(\frac{D}{\text{Mpc}} \right)^{12/13} \left(\frac{\nu_a}{5 \text{ GHz}} \right)^{-63/13} \left(\frac{t}{100 \text{ day}} \right)^{-38/13}, & \nu_a > \nu_c \end{cases}. \quad (\text{C13})$$

C.1. Temporal Scaling

The lightcurve evolution can be found from the equations above by introducing the assumption that $R \propto t^{\alpha_r}$, i.e., that the position of the shock front scales as a power law in time. Along with the assumption of a power-law density profile, $n \propto r^{-k}$, we find that $B \sim \sqrt{16\pi \epsilon_B n m_p v^2} \propto t^{-(1-\alpha_r)-\alpha_r k/2}$. Altogether, this leads to

$$\nu_a \propto \begin{cases} t^{-\frac{2(p+6)-2\alpha_r(p+8)+\alpha_r k(p+6)}{2(p+4)}} \gamma_m(t)^{\frac{2(p-2)}{p+4}}, & \nu_a < \nu_c \\ t^{\alpha_r-1-\alpha_r \frac{k(p+3)}{2(p+5)}} \gamma_m(t)^{\frac{2(p-2)[4(p+5)^2+5p]}{(2p+15)(2p+5)(p+5)}}, & \nu_a > \nu_c \end{cases} \quad (\text{C14})$$

and

$$F_a \propto \begin{cases} t^{-\frac{(2p+13)[2-\alpha_r(4-k)]}{2(p+4)}} \gamma_m(t)^{\frac{5(p-2)}{p+4}}, & \nu_a < \nu_c \\ t^{4\alpha_r-2-\alpha_r \frac{k(2p+5)}{2(p+5)}} \gamma_m(t)^{\frac{5(p-2)}{p+5}}, & \nu_a > \nu_c \end{cases}, \quad (\text{C15})$$

where the minimal electron Lorentz factor is typically constant in time, $\gamma_m \approx 1$. For shocks of sufficiently high velocity (or if the fraction of swept up electrons that

participates in diffusive-shock acceleration is very small), $\gamma_m \propto v^2 \propto t^{2(\alpha_r-1)}$. In the case of constant shock velocity ($\alpha_r = 1$) and a wind density profile ($k = 2$), we recover the well-known result in the slow-cooling regime ($\nu_a < \nu_c$), that $\nu_a \propto t^{-1}$ and $F_a \propto t^0$. In the fast-cooling regime, however, one finds that the self-absorption frequency decreases more gradually with time ($\nu_a \propto t^{-\frac{p+3}{p+5}}$) and the peak flux increases (as $F_a \propto t^{\frac{5}{p+5}}$).

The cooling frequency scales as $\nu_c \propto B^{-3} t^{-2} \propto t^{-2+3(1-\alpha_r)+3\alpha_r k/2}$, so that the ratio of self-absorption to cooling frequency evolves as









$$\frac{\nu_a}{\nu_c} \propto \begin{cases} t^{-\frac{(4\alpha_r-2)(p+5)-\alpha_r k(2p+9)}{p+4}}, & \nu_a < \nu_c \\ t^{-\frac{(4\alpha_r-2)(p+5)-\alpha_r k(2p+9)}{p+5}}, & \nu_a > \nu_c \end{cases}. \quad (\text{C16})$$

This increases with time if $k < (4\alpha_r - 2)(p + 5)/\alpha_r(2p + 9) \approx 1.1(2 - 1/\alpha_r)$, that is, if the ambient density profile is relatively shallow and the shock does not decelerate too dramatically ($\alpha_r \approx 1$).

Overall, for the fiducial case where $\gamma_m \approx 1$, the lightcurve evolution at a given frequency scales as

$$f_\nu = F_a \begin{cases} \left(\frac{\nu_*}{\nu_a} \right)^{-\frac{p-1}{2}} \left(\frac{\nu}{\nu_*} \right)^{-\frac{p}{2}}, & \nu > \nu_* \equiv \max(\nu_c, \nu_a) \\ \left(\frac{\nu}{\nu_a} \right)^{-\frac{p-1}{2}}, & \nu_a < \nu < \nu_c \\ \left(\frac{\nu}{\nu_a} \right)^{5/2}, & \nu < \nu_a \end{cases} \quad \begin{cases} t^{-[2(p+4)+\alpha_r k(p+2)-2\alpha_r(p+8)]/4}, & \nu > \max(\nu_c, \nu_a) \\ t^{-[(2+\alpha_r k)(p+5)-2\alpha_r(p+11)]/4}, & \nu_a < \nu < \nu_c \\ t^{-[2+\alpha_r(k+6)]/4}, & \nu < \nu_a \end{cases}. \quad (\text{C17})$$

ORCID iDs

Anna Y. Q. Ho  <https://orcid.org/0000-0002-9017-3567>
 Ben Margalit  <https://orcid.org/0000-0001-8405-2649>
 Daniel A. Perley  <https://orcid.org/0000-0001-8472-1996>
 Yuhang Yao  <https://orcid.org/0000-0001-6747-8509>
 Dougal Dobie  <https://orcid.org/0000-0003-0699-7019>
 David L. Kaplan  <https://orcid.org/0000-0001-6295-2881>
 Andrew O'Brien  <https://orcid.org/0000-0003-4609-2791>
 Andrew Zic  <https://orcid.org/0000-0002-9583-2947>

References

- Abazajian, K., Addison, G., Adshead, P., et al. 2019, arXiv:1907.04473
- Alexander, K. D., Berger, E., Guillochon, J., Zauderer, B. A., & Williams, P. K. G. 2016, *ApJL*, **819**, L25
- Alexander, K. D., van Velzen, S., Horesh, A., & Zauderer, B. A. 2020, *SSRv*, **216**, 81
- Arnaud, K. A. 1996, in ASP Conf. Ser. 101, *Astronomical Data Analysis Software and Systems V*, ed. G. H. Jacoby & J. Barnes (San Francisco, CA: ASP), 17
- Astropy Collaboration, Price-Whelan, A. M., Sipőcz, B. M., et al. 2018, *AJ*, **156**, 123
- Astropy Collaboration, Robitaille, T. P., Tollerud, E. J., et al. 2013, *A&A*, **558**, A33
- Bellm, E. C., Kulkarni, S. R., Graham, M. J., et al. 2019, *PASP*, **131**, 018002
- Berger, E., Zauderer, A., Pooley, G. G., et al. 2012, *ApJ*, **748**, 36
- Bietenholz, M. F., Bartel, N., Argo, M., et al. 2021, *ApJ*, **908**, 75
- Blandford, R., & Eichler, D. 1987, *PhR*, **154**, 1
- Bright, J., Wieringa, M., Laskar, T., et al. 2020a, *ATel*, **14148**, 1
- Bright, J., Wieringa, M., Margutti, R., et al. 2020b, *ATel*, **14249**, 1
- Bright, J. S., Margutti, R., Matthews, D., et al. 2022, *ApJ*, **926**, 112
- Caprioli, D., Haggerty, C. C., & Blasi, P. 2020, *ApJ*, **905**, 2
- Carlstrom, J. E., Ade, P. A. R., Aird, K. A., et al. 2011, *PASP*, **123**, 568
- Cash, W. 1979, *ApJ*, **228**, 939
- Chandra, P., & Frail, D. A. 2012, *ApJ*, **746**, 156
- Chevalier, R. A. 1998, *ApJ*, **499**, 810
- Chevalier, R. A., & Fransson, C. 2006, *ApJ*, **651**, 381
- Cohen, A. S., Clarke, T. E., Ferretti, L., & Kassim, N. E. 2005, *ApJL*, **620**, L5
- Coppejans, D. L., Margutti, R., Terreran, G., et al. 2020, *ApJL*, **895**, L23
- Cordes, J. M., & Lazio, T. J. W. 2002, arXiv:astro-ph/0207156
- Corsi, A., Ofek, E. O., Gal-Yam, A., et al. 2014, *ApJ*, **782**, 42
- de Ugarte Postigo, A., Lundgren, A., Martín, S., et al. 2012, *A&A*, **538**, A44
- Dong, D. Z., Hallinan, G., Nakar, E., et al. 2021, *Sci*, **373**, 1125
- Eftekhari, T., Berger, E., Metzger, B. D., et al. 2021, arXiv:2110.05494
- Eftekhari, T., Berger, E., Zauderer, B. A., Margutti, R., & Alexander, K. D. 2018, *ApJ*, **854**, 86
- Eichler, D., & Granot, J. 2006, *ApJL*, **641**, L5
- Frater, R. H., Brooks, J. W., & Whiteoak, J. B. 1992, *JEEPA*, **12**, 103
- Fruscione, A., McDowell, J. C., Allen, G. E., et al. 2006, *Proc. SPIE*, **6270**, 62701V
- Gaia Collaboration, Brown, A. G. A., Vallenari, A., et al. 2018, *A&A*, **616**, A1
- Giannios, D., & Spitkovsky, A. 2009, *MNRAS*, **400**, 330
- Graham, M. J., Kulkarni, S. R., Bellm, E. C., et al. 2019, *PASP*, **131**, 078001
- Granot, J., & Sari, R. 2002, *ApJ*, **568**, 820
- Guns, S., Foster, A., Daley, C., et al. 2021, *ApJ*, **916**, 98
- Ho, A. Y. Q., Goldstein, D. A., Schulze, S., et al. 2019a, *ApJ*, **887**, 169
- Ho, A. Y. Q., Perley, D. A., Beniamini, P., et al. 2020a, *ApJ*, **905**, 98
- Ho, A. Y. Q., Perley, D. A., Gal-Yam, A., et al. 2021, arXiv:2105.08811
- Ho, A. Y. Q., Perley, D. A., Kulkarni, S. R., et al. 2020b, *ApJ*, **895**, 49
- Ho, A. Y. Q., Perley, D. A., & Yao, Y. 2020c, *TNSAN*, **204**, 1
- Ho, A. Y. Q., Phinney, E. S., Ravi, V., et al. 2019b, *ApJ*, **871**, 73
- Ho, P. T. P., Moran, J. M., & Lo, K. Y. 2004, *ApJL*, **616**, L1
- Högbom, J. A. 1974, *A&AS*, **15**, 417
- Horesh, A., Cenko, S. B., Perley, D. A., et al. 2015, *ApJ*, **812**, 86
- Horesh, A., Stockdale, C., Fox, D. B., et al. 2013, *MNRAS*, **436**, 1258
- Hunter, J. D. 2007, *CSE*, **9**, 90
- Jóhannesson, G., & Björnsson, G. 2018, *ApJL*, **859**, L11
- Kashiyama, K., Hotokezaka, K., & Murase, K. 2018, *MNRAS*, **478**, 2281
- Krauss, M. I., Soderberg, A. M., Chomiuk, L., et al. 2012, *ApJL*, **750**, L40
- Kuin, N. P. M., Wu, K., Oates, S., et al. 2019, *MNRAS*, **487**, 2505
- Kulkarni, S. R., Frail, D. A., Wieringa, M. H., et al. 1998, *Natur*, **395**, 663
- Laskar, T., Berger, E., Margutti, R., et al. 2018, *ApJ*, **859**, 134
- Laskar, T., van Eerten, H., Schady, P., et al. 2019, *ApJ*, **884**, 121
- Law, C. J., Gaensler, B. M., Metzger, B. D., Ofek, E. O., & Sironi, L. 2018, *ApJL*, **866**, L22
- Leung, S.-C., Fuller, J., & Nomoto, K. 2021, *ApJ*, **915**, 80
- Maeda, K., Chandra, P., Matsuoka, T., et al. 2021, *ApJ*, **918**, 34
- Mahadevan, R., Narayan, R., & Yi, I. 1996, *ApJ*, **465**, 327
- Margalit, B., & Quataert, E. 2021, *ApJL*, **923**, L14
- Margutti, R., Metzger, B. D., Chornock, R., et al. 2019, *ApJ*, **872**, 18
- Margutti, R., Soderberg, A. M., Wieringa, M. H., et al. 2013, *ApJ*, **778**, 18
- Matthews, D., Margutti, R., Brethauer, D., et al. 2020, *ATel*, **14154**, 1
- McMullin, J. P., Waters, B., Schiebel, D., Young, W., & Golap, K. 2007, in ASP Conf. Ser. 376, *CASA Architecture and Applications*, ed. R. A. Shaw, F. Hill, & D. J. Bell (San Francisco, CA: ASP), 127
- Metzger, B. D., Williams, P. K. G., & Berger, E. 2015, *ApJ*, **806**, 224
- Mooley, K. P., Margalit, B., Law, C. J., et al. 2022, *ApJ*, **924**, 16
- Naess, S., Battaglia, N., Bond, J. R., et al. 2021, *ApJ*, **915**, 14
- Narayan, R. 1992, *RSPTA*, **341**, 151
- Nayana, A. J., & Chandra, P. 2021, *ApJL*, **912**, L9
- Ofek, E. O., Rabinak, I., Neill, J. D., et al. 2010, *ApJ*, **724**, 1396
- Özel, F., Psaltis, D., & Narayan, R. 2000, *ApJ*, **541**, 234
- Park, J., Caprioli, D., & Spitkovsky, A. 2015, *PhRvL*, **114**, 085003
- Perley, D., Schulze, S., & Bruch, R. 2020a, *TNSAN*, **37**, 1
- Perley, D. A., Cenko, S. B., Corsi, A., et al. 2014, *ApJ*, **781**, 37
- Perley, D. A., Ho, A. Y. Q., Fremling, C., & Yao, Y. 2020b, *ATel*, **14105**, 1
- Perley, D. A., Ho, A. Y. Q., Yao, Y., et al. 2021, *MNRAS*, **508**, 5138
- Perley, D. A., Mazzali, P. A., Yan, L., et al. 2019, *MNRAS*, **484**, 1031
- Perley, D. A., Schulze, S., & de Ugarte Postigo, A. 2017, *GCN*, **22252**, 1
- Perley, R. A., Chandler, C. J., Butler, B. J., & Wrobel, J. M. 2011, *ApJL*, **739**, L1
- Planck Collaboration, Ade, P. A. R., Aghanim, N., et al. 2016, *A&A*, **594**, A13
- Prentice, S. J., Maguire, K., Smartt, S. J., et al. 2018, *ApJL*, **865**, L3
- Quataert, E., Lecoanet, D., & Coughlin, E. R. 2019, *MNRAS*, **485**, L83
- Ressler, S. M., & Laskar, T. 2017, *ApJ*, **845**, 150
- Rest, A., Garnavich, P. M., Khatami, D., et al. 2018, *NatAs*, **2**, 307
- Rickett, B. J. 1990, *ARA&A*, **28**, 561
- Rivera Sandoval, L. E., Maccarone, T. J., Corsi, A., et al. 2018, *MNRAS*, **480**, L146
- Rybicki, G. B., & Lightman, A. P. 1986, *Radiative Processes in Astrophysics* (New York: Wiley-VCH)
- Salas, P., Bauer, F. E., Stockdale, C., & Prieto, J. L. 2013, *MNRAS*, **428**, 1207
- Sault, R. J., Teuben, P. J., & Wright, M. C. H. 1995, in ASP Conf. Ser. 77, *Astronomical Data Analysis Software and Systems IV*, ed. R. A. Shaw, H. E. Payne, & J. J. E. Hayes (San Francisco, CA: ASP), 433
- Sheth, K., Frail, D. A., White, S., et al. 2003, *ApJL*, **595**, L33
- Shulevski, A., Morganti, R., Barthel, P. D., et al. 2015, *A&A*, **583**, A89
- Sironi, L., & Giannios, D. 2013, *ApJ*, **778**, 107
- Smith, N. 2014, *ARA&A*, **52**, 487
- Soderberg, A. M., Chakraborti, S., Pignata, G., et al. 2010, *Natur*, **463**, 513
- Soderberg, A. M., Chevalier, R. A., Kulkarni, S. R., & Frail, D. A. 2006a, *ApJ*, **651**, 1005
- Soderberg, A. M., Kulkarni, S. R., Berger, E., et al. 2005, *ApJ*, **621**, 908
- Soderberg, A. M., Kulkarni, S. R., Nakar, E., et al. 2006b, *Natur*, **442**, 1014
- Soderberg, A. M., Nakar, E., Berger, E., & Kulkarni, S. R. 2006c, *ApJ*, **638**, 930
- Thornton, R. J., Ade, P. A. R., Aiola, S., et al. 2016, *ApJS*, **227**, 21
- van Dyk, S. D., Weiler, K. W., Sramek, R. A., & Panagia, N. 1993, *ApJL*, **419**, L69
- Virtanen, P., Gommers, R., Oliphant, T. E., et al. 2020, *NatMe*, **17**, 261
- Walker, M. A. 1998, *MNRAS*, **294**, 307
- Warren, D. C., Barkov, M. V., Ito, H., Nagataki, S., & Laskar, T. 2018, *MNRAS*, **480**, 4060
- Weiler, K. W., Sramek, R. A., Panagia, N., van der Hulst, J. M., & Salvati, M. 1986, *ApJ*, **301**, 790
- Weiler, K. W., van Dyk, S. D., Panagia, N., Sramek, R. A., & Discenna, J. L. 1991, *ApJ*, **380**, 161
- Weiler, K. W., Williams, C. L., Panagia, N., et al. 2007, *ApJ*, **671**, 1959
- Whitehorn, N., Natoli, T., Ade, P. A. R., et al. 2016, *ApJ*, **830**, 143
- Willingale, R., Starling, R. L. C., Beardmore, A. P., Tanvir, N. R., & O'Brien, P. T. 2013, *MNRAS*, **431**, 394
- Wilms, J., Allen, A., & McCray, R. 2000, *ApJ*, **542**, 914
- Yuan, Q., Wang, Q. D., Lei, W.-H., Gao, H., & Zhang, B. 2016, *MNRAS*, **461**, 3375
- Zauderer, B. A., Berger, E., Soderberg, A. M., et al. 2011, *Natur*, **476**, 425